Int. J. Solids Structures Vol. 24, No. 5, pp. 505–535, 1988
Printed in Great Britain.

0020-7683/88 $3.00+.00

ON THE COLLAPSE OF INELASTIC TUBES UNDER COMBINED BENDING AND PRESSURE

E. CORONA and S. KYRIAKIDES
Department of Aerospace Engineering and Engineering Mechanics, University of Texas at Austin, Austin, TX 78712, U.S.A.

(*Received* 6 *August* 1987; *in revised form* 2 *October* 1987)

Abstract—The response and stability of long, relatively thick-walled metal tubes under combined bending and external pressure were studied through combined experimental and numerical efforts. The experiments involved stainless steel 304 tubes with nominal diameter to thickness ratios of 34.7 and 24.5. Curvature–pressure interaction collapse envelopes were generated for two different loading paths involving bending followed by pressure and pressure followed by bending. The tube response, the critical collapse loads and the nature of the instabilities observed were found to depend on the loading path. A suitable formulation of the problem based on the principle of virtual work was used to numerically simulate the experiments. The J_2 flow rule of plasticity was used to model the inelastic material behavior. The analysis successfully reproduced the limit load type of instabilities which govern the problem in the range of diameter to thickness ratios of interest.

NOMENCLATURE

D	tube outside diameter
D_0	tube mean diameter, $(D_{\max}+D_{\min}-2t)/2$
ΔD	change in diameter in plane of bending
E	Young's modulus
J_2	second invariant of deviatoric stress tensor
M	bending moment
M_0	$\sigma_0 D_0^2 t$
n	Ramberg–Osgood hardening parameter
P	pressure
P_{co}	collapse pressure
P_0	yield pressure
P_p	propagation pressure
R	tube mean radius
S, S_r, S_θ	anisotropy parameters
t	tube thickness
v, w	displacements
w_0	initial imperfection
x, z	coordinates
α_{ij}	back stress tensor components
Δ_0	imperfection amplitude, $(D_{\max}-D_{\min})/(D_{\max}+D_{\min})$
ε_{ij}	strain tensor components
$\varepsilon, \varepsilon_x, \varepsilon_\theta$	strain components
$\varepsilon_x^0, \varepsilon_\theta^0$	strain components at "mid-surfaces"
ζ	distance from tube center plane to points in the tube cross section
θ	coordinate
κ	tube curvature
κ_1	t/D_0^2
κ_θ	local circumferential curvature
ν	Poisson's ratio
$\sigma, \sigma_x, \sigma_\theta$	stress components
σ_e	equivalent stress
σ_y	Ramberg–Osgood yield parameter
σ_0, σ_{0x}	yield stress in axial direction
$\sigma_{0\theta}, \sigma_{0r}$	yield stress in circumferential and radial directions.

INTRODUCTION

The work presented in this paper is motivated by the design needs of structures such as pipelines and risers in deep offshore waters. The high ambient pressure makes such structures collapse critical. They are particularly vulnerable during the installation process when, in addition to the external pressure, they must sustain bending and/or tension loads[1]. An example of a pipeline installation process is shown in Fig. 1(a). The line is payed into the sea off a special lay vessel. The configuration of the suspended section induces bending which is usually highest in the "sagbend" region close to the seafloor. The bending curvature induced is controlled by the tension applied at the barge. Thus, sufficient tension must be applied to avoid collapse of the line.

Another collapse sensitive installation procedure is the one in which a pipeline on the seafloor is pulled through a "J"-tube of fixed radius (Fig. 1(a)). The design of the J-tube must, by necessity, be strongly influenced by the pipe collapse limitations. The pressure–curvature loading history induced to a safely designed pipeline by the two processes described is shown schematically in Fig. 1(b). The collapse envelope of the pipe is included for reference. The paper addresses the problem of establishing such collapse envelopes for pipe geometric and material parameters suitable for deep waters (1500–8000 ft; 450–2450 m).

Brazier[2] pointed out that the response of long elastic tubes in pure bending is characterized by a limit load type of instability (see also Ref. [3]). The limit moment is directly related to the ovalization experienced by the tube cross section. Bifurcation type of instability characterized by axial and circumferential waves was shown to often precede the limit load[4–7]. In the presence of external pressure, the tube non-linear response becomes softer. This leads to lower limit moments and bifurcation loads[7, 8].

In the case of thicker shells ($10 < D_0/t < 200$) both the response as well as the inherent instabilities of the structure are strongly influenced by the interaction of the induced ovalization and the plastic characteristics of the material. Ades[9], obtained the limit moment of elastoplastic tubes by assuming the ovalized cross section to be elliptical and by modeling inelastic behavior through the J_2 deformation theory of plasticity. Gellin[10], developed a more systematic solution procedure for establishing the non-linear tube response by adopting circumferentially inextensional kinematics and the J_2 deformation

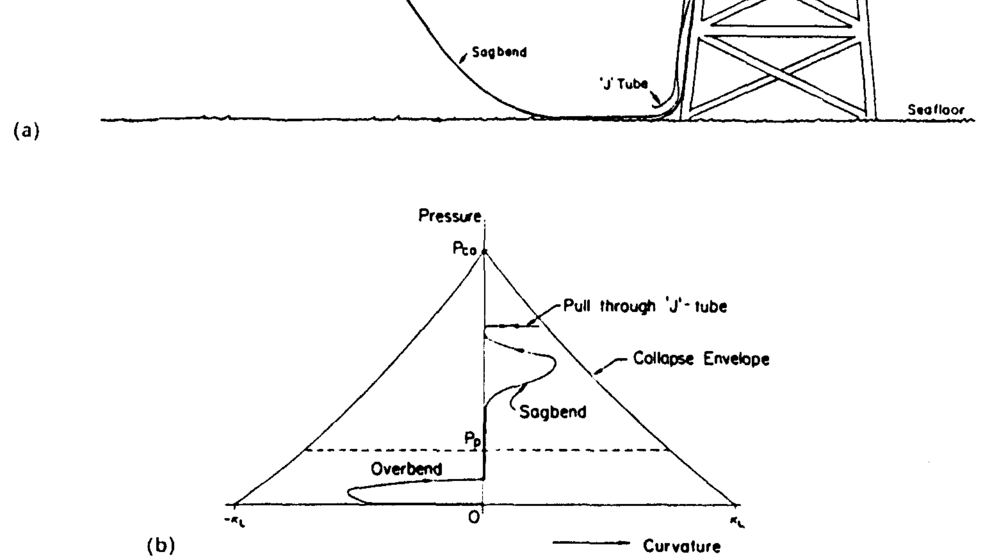

Fig. 1. (a) The "S"-lay method and pull through the "J"-tube. (b) Pressure–curvature loading history.

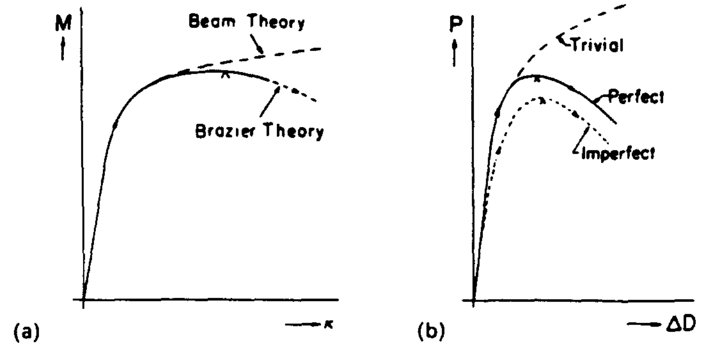

Fig. 2. (a) Moment-curvature response for inelastic tubes. (b) Pressure-deflection responses for inelastic tubes.

theory of plasticity. Gellin's solution procedure was extended in Ref. [11] by adopting a set of extensional kinematics and a variety of incremental plasticity models. Other noteworthy contributions to the problem are those of Bushnell[12] and Calladine[13]. Experiments involving pure bending of inelastic shells have been reported in Refs [14–20]. From these studies it can be concluded that for "thinner" tubes bifurcation type of instability precedes the limit load; for "thicker" tubes the limit load is reached first as shown in Fig. 2(a). For commonly used steel and aluminum alloys the transition seems to be between D/t values of 35–45.

Long, relatively thick-walled tubes under external pressure experience a limit pressure type of instability. Unlike the limit moment in the pure bending loading problem, the limit pressure is very sensitive to initial geometric imperfections, particularly initial ovality (Fig. 2(b)). Detailed parametric studies of the collapse pressure (and literature review) can be found in Refs [21, 22].

References [23, 24] reported experiments involving collapse of tubes under combined bending and external pressure. The results of Ref. [23] were for steel pipes having D/t values of 40, 60 and 80; those of Ref. [24] for aluminum tubes with D/t values of 35 and 50. A shell bifurcation type of analysis of the problem was developed in Ref. [23], and an analysis for predicting the limit load type of instability of the problem was presented in Ref. [25]. Both analyses adopted the J_2 deformation theory of plasticity to model the inelastic material behavior. Fabian[26] developed a more complete analysis of the problem involving both bifurcation and limit load instabilities and the more appropriate J_2 incremental plasticity model.

The objective of this study is to extend the experimental data, as well as the analytical tools available for establishing the collapse of tubes under combined bending and external pressure, to low D/t values. The D/t range of 35–15 was chosen as the one most relevant to deep offshore applications. For common steel alloy tubes in this D/t range, collapse is governed primarily by limit load type instabilities for both external pressure as well as pure bending loads. In addition, extensive plastic deformations can precede collapse. As a result the critical combinations of pressure and bending are expected to be dependent on the loading path followed to collapse[27].

A combined bending and pressure facility capable of testing steel tubes in the range of interest was developed. Collapse experiments for two values of D/t and three loading paths are presented. A suitable problem formulation is also presented followed by a comparison between experimental and predicted results and a limited parametric study.

EXPERIMENTS

Test facilities

The combined bending-pressure experiments were carried out in a specially designed test facility shown in Fig. 3(a). It consists of a pure bending device which can operate inside a pressure vessel. A data acquisition system is used to monitor the experiments.

The bending device is shown schematically in Fig. 4(a). It was designed as a four point bending machine capable of applying bending and reverse bending (design similar to facilities in Refs [20, 24]). It consists of two heavy sprocket assemblies resting on two beams. Heavy chains run around the sprockets and are connected to two hydraulic cylinders and load cells forming a closed loop. Each tube tested is fitted with solid rod extensions as shown in Fig. 4(b). The rods are chamfered at the ends to reduce stress concentrations and to avoid premature buckling at the end of the test specimen. The rod–tube interface is sealed with a rubber hose. The test specimen assembly is engaged by the bending device through four rollers located on each sprocket, as shown in Fig. 4(b).

Bending is achieved by contracting either of the cylinders causing rotation of the sprockets. The load transfer to the test specimen is in the form of a couple formed by concentrated loads from two of the rollers. During bending the rolling contact between the test specimen and the device guarantees freedom of movement of the tube in the axial direction.

The hydraulic system was designed such that the idle cylinder extends an amount equal to the contraction of the active one. This ensures that the periphery of the closed loop consisting of the chains, load cells and cylinders has constant length. Bending in the reverse sense is achieved by reversing the direction of flow in the hydraulic circuit. The hydraulic system is such that the device operates essentially as a curvature controlled testing machine.

The curvature of the test specimen is directly proportional to the sum of the angles of rotation of the sprockets. A rotary variable differential transformer (RVDT) is used to monitor the rotation of each sprocket. The curvature range of the set-up is governed by the diameter of the pressure vessel and the length of the test specimen.

The applied bending moment is directly proportional to the tension in the chain which is monitored by the two load cells in the chain loop. The electrical circuits of the load cells were designed so that the measured load is insensitive to pressure and temperature changes, and negates the effect of the weight of the chain loop. The capacity of the bending device is 15,000 lb in. (1700 N m). Tubes having maximum length of 40 in. (1.0 m) and diameters up to 1.5 in. (38 mm) can be tested.

The device was designed to be stiff relative to the test specimen. For the experiments reported, the energy stored in the device was less than 3% of the energy stored in the test specimen.

A special lightweight instrument mounted at a point close to the tube midspan was used to monitor changes in the major and minor diameters of the tube cross section.

The pressure vessel is cylindrical in shape, 72 in. (1.8 m) long and has an internal diameter of 20 in. (0.51 m). A special closure system provides full opening access at one end of the vessel (Fig. 3(a)). The vessel has a working pressure of 5000 psi (350 bar). The bending device rolls into the pressure vessel and is operated remotely. The operational set-up of the test facility is shown schematically in Fig. 3(b). The pressure vessel is usually completely filled with water and pressurized in a nearly volume controlled fashion using a hydraulic pump. Pressure gages and an electrical pressure transducer are used to monitor the pressure during the experiment. All transducers, signal cables and hydraulic lines operating in the wet and high pressure environment of the pressure vessel had to be specially designed, insulated and sealed.

A computer operated data acquisition system was used to monitor the experiment. The applied moment (M), curvature (κ), ovalization ($\Delta D/D$) and pressure (P) were customarily monitored. The signals from the corresponding transducers were suitably amplified and digitized through an A/D converter at the rate of about 5 sample sets per second. A microcomputer was used to select, manipulate, display and store the data in sets of $\{M, \kappa, \Delta D/D, P\}$. Approximately 1500 data sets were recorded for each typical bending–pressure collapse experiment. The recorded data had uncertainties of 3% for the moment, 5% for the curvature, 0.5% for the ovalization and 0.5% for the pressure.

Experimental procedure

The experiments were carried out using seamless, drawn, stainless steel tubes having nominal diameters of 1.25 in. (31.8 mm). Results for nominal D_0/t values of 34.7 and 24.5

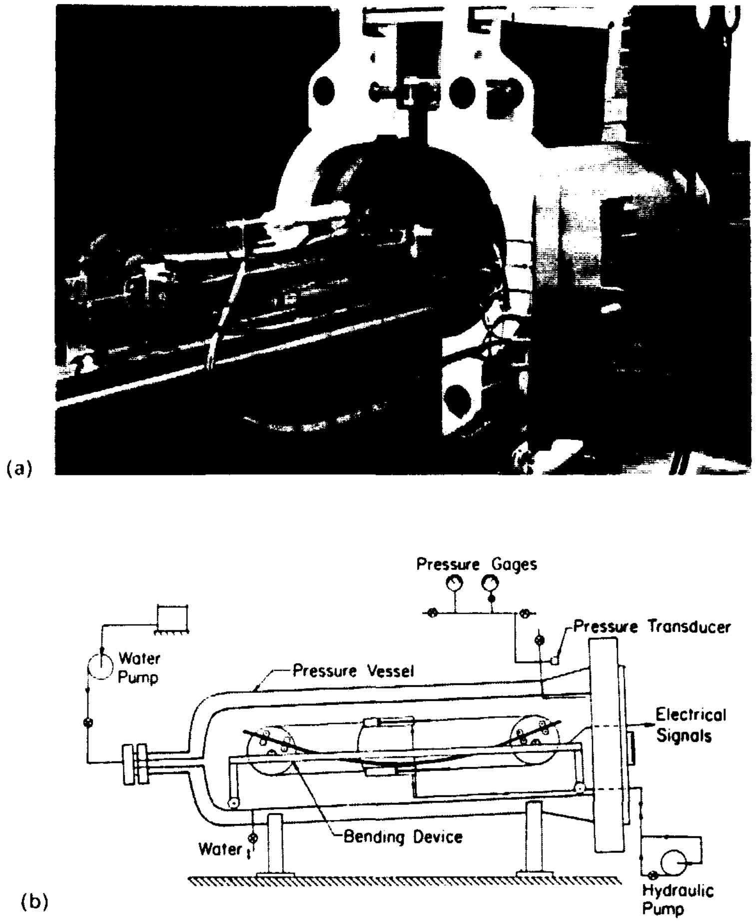

Fig. 3. (a) Combined pressure bending test facility. (b) Test facility in operation (schematic).

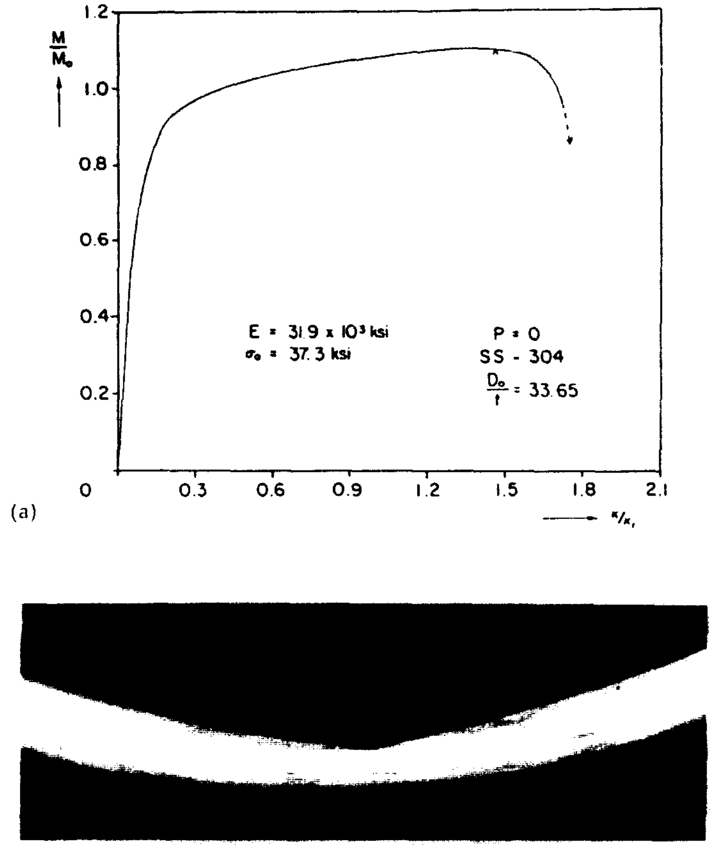

Fig. 6. (a) Measured moment–curvature response (pure bending case). (b) Localized collapse mode.

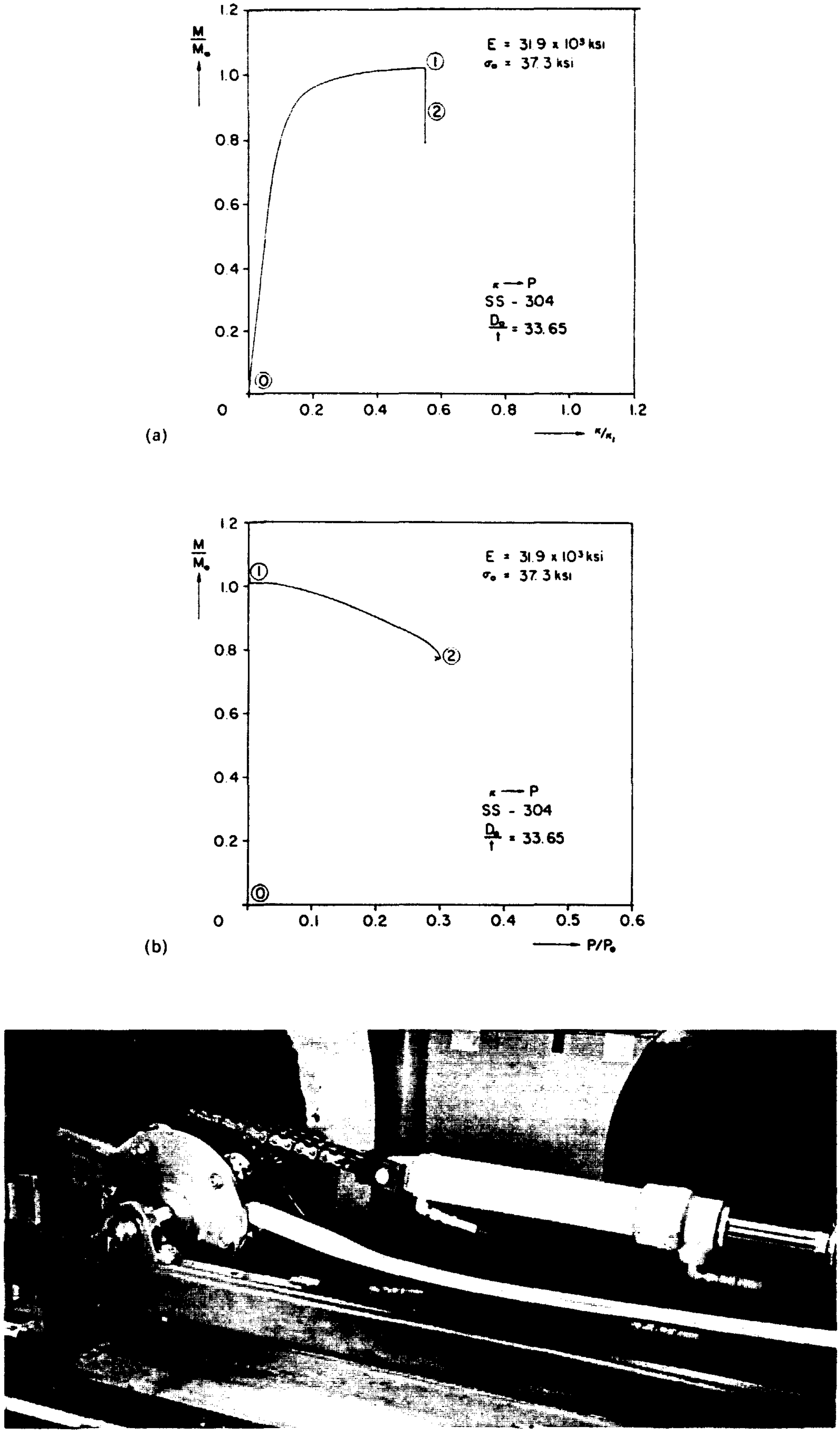

Fig. 8. (a) Moment curvature response. (b) Moment-pressure response. (c) Collapsed specimen.

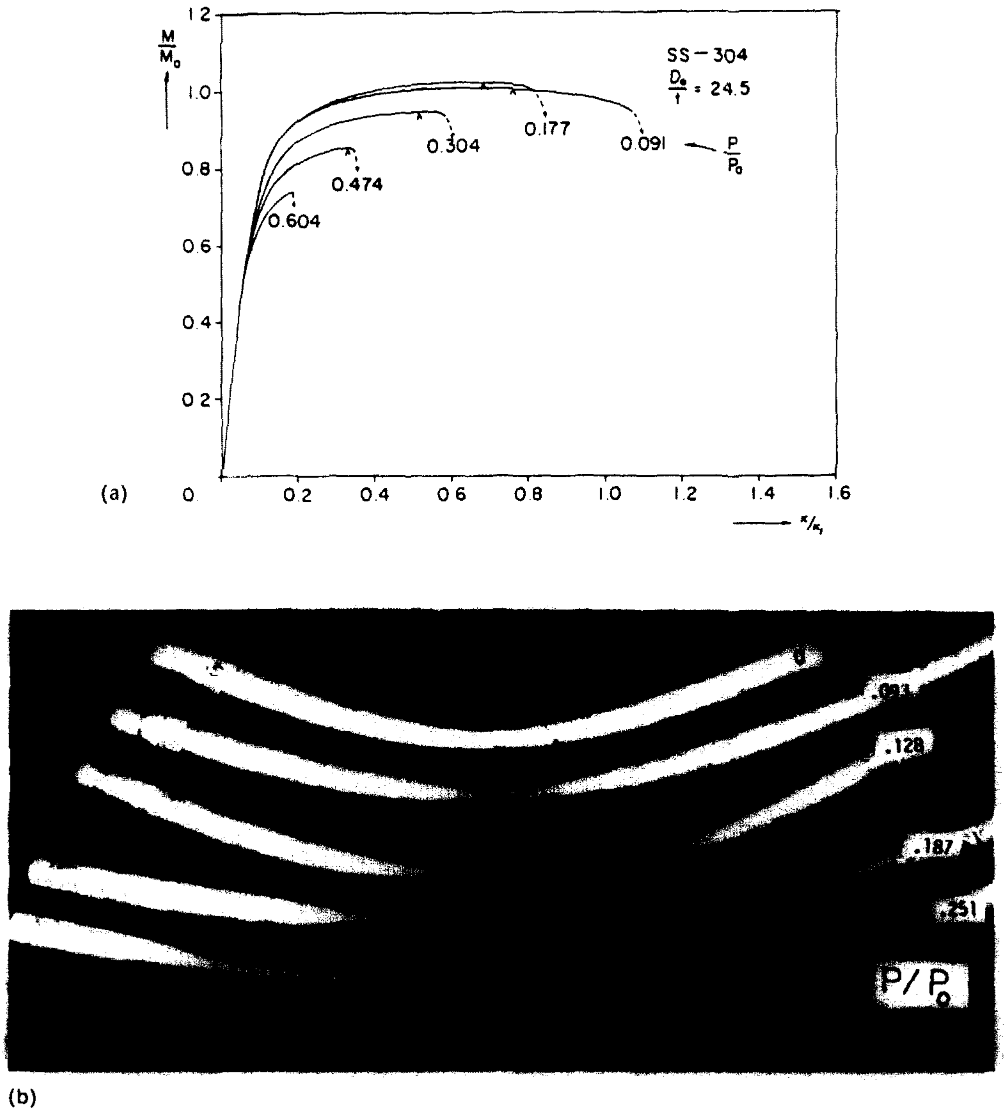

Fig. 9. (a) Measured moment–curvature responses for different values of pressure. (b) Test specimens collapsed at different pressures (and curvatures).

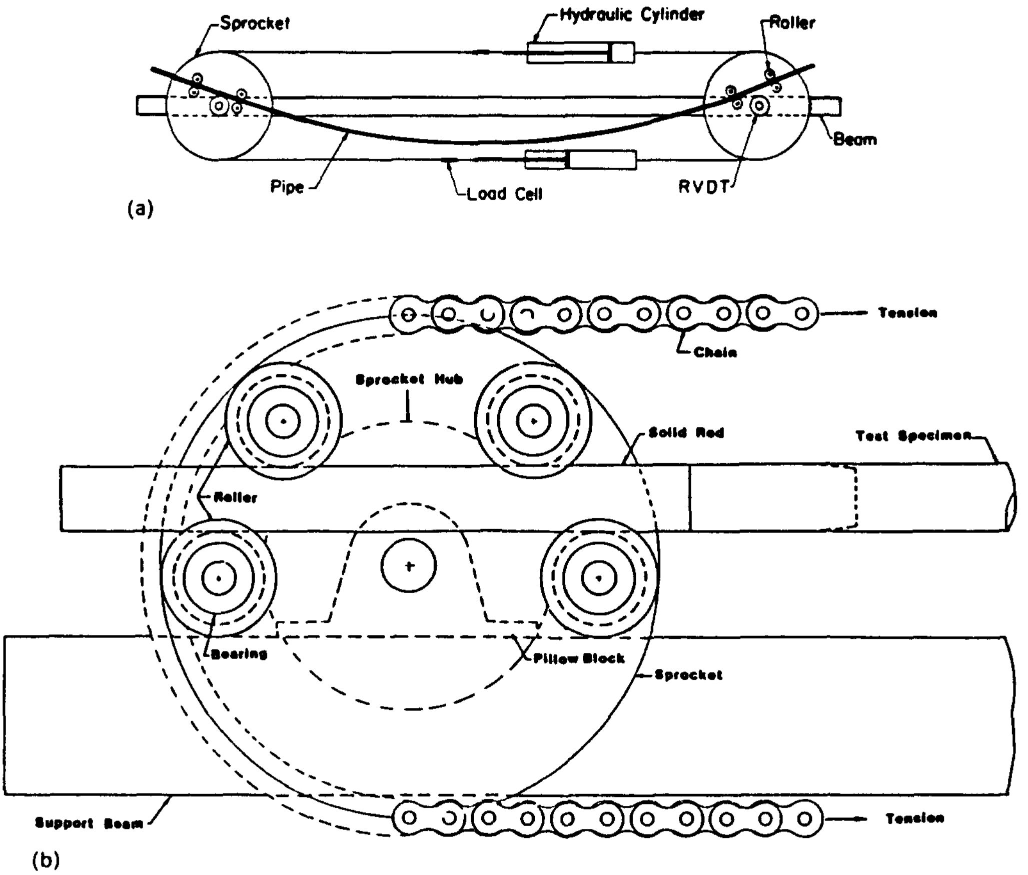

Fig. 4. (a) Schematic of pure bending device. (b) Load transfer assembly.

are presented. The lengths of the test specimens ranged between 18 and 24 tube diameters. The material properties of the tubes tested were obtained from uniaxial tension tests performed on axial test coupons cut from sections adjacent to the test specimens. Previous experience with this type of tubes[21] indicated that the manufacturing process could induce inelastic anisotropy to the tubes. The main characteristic of the anisotropy was that the yield stress in the circumferential direction was different from that in the axial direction. Biaxial experiments involving combined internal pressure and axial loading were carried out on sections of tubes in order to establish the degree of anisotropy (see Ref. [28] for details).

The mean initial geometric imperfections of each test specimen were established by micrometer measurements prior to each test. These included initial ovality and thickness variation measurements. The mean values of the material and geometric parameters of the two families of tubes tested are listed in Table 1.

The combined bending-pressure test facility used in the experiments allows inde-

Table 1. Geometric and material parameters of tubes tested

D_0/t (Nominal)	D, in. (mm)	t, in. (mm)	Δ_0	E, ksi (GPa)	σ_y, ksi (MPa)	σ_0, ksi (MPa)	n	S
34.7	1.2480 (31.70)	0.0357 (0.907)	0.4×10^{-3}	26.9×10^3 (186)	32.5 (224)	37.6 (259)	9.67	0.94
24.5	1.2475 (31.69)	0.0485 (1.232)	1.0×10^{-3}	29.2×10^3 (201)	49.6 (342)	51.8 (357)	17	0.80

pendent control of the applied curvature and external pressure. Three loading paths were adopted in the experiments; they are shown schematically in Fig. 5. In the first loading path (Fig. 5(a)), the tube was first bent to a chosen value of curvature at zero pressure. The curvature was then fixed and pressure loading was applied until the tube collapsed (depicted as $\kappa \rightarrow P$ loading path). In the second (Fig. 5(b)), pressure was applied first followed by bending under constant pressure until collapse (depicted by $P \rightarrow \kappa$ loading path). In the third, the curvature and pressure were incremented alternately by small steps forming a nearly radial path as shown in Fig. 5(c) (depicted as "radial" loading path). This was continued until the tube collapsed.

For the first two loading paths enough experiments were carried out to establish the configuration of the collapse envelopes for the full range of pressure and curvature values of interest. In the case of the "radial" path a selected number of experiments were carried out in order to establish the trend of the results.

Definition of collapse

The geometric and material parameters of the two families of tubes tested (Table 1) were such that in a pure pressure test the bifurcation pressure of the tubes with $D_0/t = 34.7$ occurred in the elastic range; that of the tubes with $D_0/t = 24.5$ occurred in the plastic range. However, the presence of initial geometric imperfections combined with inelastic effects led to limit load instabilities which were in general lower than the bifurcation pressures. The tubes collapsed catastrophically on attainment of the limit pressures.

The pure bending moment–curvature responses of both families of tubes tested were characterized by limit moments (Fig. 6(a)). Bending was carried out under curvature controlled conditions and, as a result, the tubes could be bent beyond their limit moments. However, soon after the limit moment was achieved the ovalization of the cross section ceased to be uniform along the length of the tube. Deformation was localized in a region 5–6 diameters long as shown in Fig. 6(b); this was accompanied by a sharp decline in

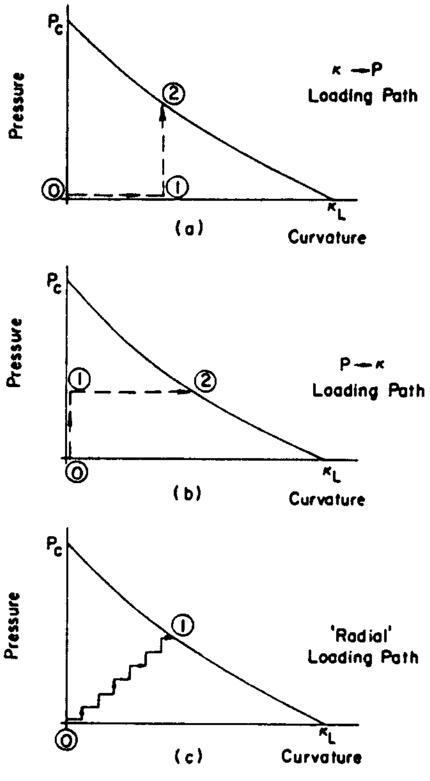

Fig. 5. Loading paths considered.

moment bearing capacity. The limit moment will be taken as one of the critical collapse criteria.

The collapse mechanism under combined bending and pressure was found to depend on the loading history. The variation of the tube moment, curvature, ovalization and pressure during the two parts of the $\kappa \rightarrow P$ and $P \rightarrow \kappa$ loading paths are shown schematically in Fig. 7. In a typical $\kappa \rightarrow P$ experiment the tube was first bent to a curvature κ_1 with corresponding moment M_1 and ovalization ΔD_1 (Figs 7(a) (i) and (ii)). The curvature was fixed at the value κ_1 and the pressure gradually increased. This led to an increase in ovalization and a drop in moment (Figs 7(a) (iii) and (iv)). This continued until the ovalization grew to a value at which the applied pressure could no longer be supported and the tube collapsed. This is identified by the limit pressure (collapse pressure, P_{co}) in Fig. 7(a) (iii). Measured moment, curvature and pressure values for such a path are shown in Figs 8(a) and (b). Figure 8(c) shows a test specimen after collapse.

In a typical $P \rightarrow \kappa$ loading history (Fig. 7(b)) pressure P_1 was applied first. This induced a small change in the geometry of the cross section indicated by ΔD_1. The tube curvature was then gradually increased while the pressure was kept constant at the value of P_1. The

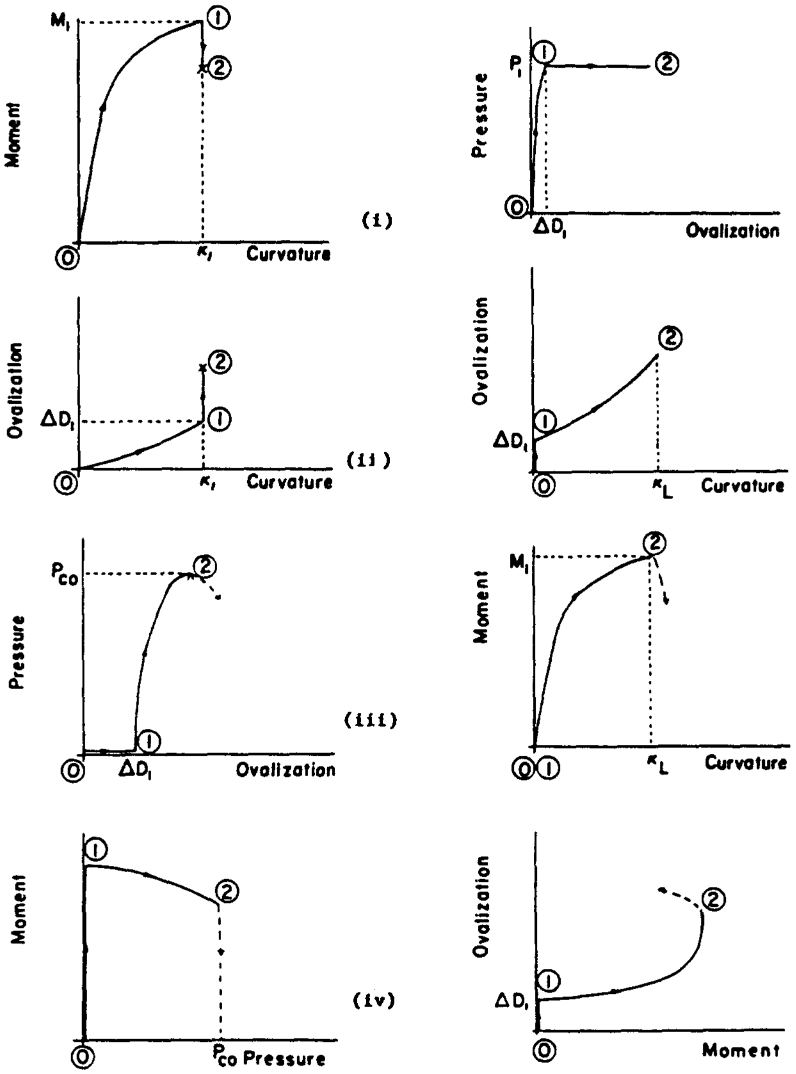

(a) κ→P Loading Path (b) P→κ Loading Path

Fig. 7. Responses for two loading paths.

prescribed bending induced a growth of ovalization of the tube cross section as shown in Figs 7(b) (ii) and (iv). The rate of growth of ovalization was accelerated by the presence of the pressure. Eventually a limit moment was reached (Fig. 7(b) (iii)). Because of the accelerated growth of ovalization the limit moment (M_2) and the corresponding limit curvature (κ_2) were smaller than the critical values at lower pressures. For "higher" values of pressure, collapse followed immediately the attainment of the limit moment. For "lower" values of pressure, bending beyond the limit moment was possible. Such loading led to localized growth of ovalization and eventually to catastrophic collapse.

Figure 9(a) shows a set of measured moment–curvature responses for different values of pressure. Figure 9(b) shows a set of collapsed test specimens. The extent of damage sustained by a test specimen during collapse depends on the value of pressure and the compliance of the pressure vessel.

PROBLEM FORMULATION

The response and collapse, of the tubes of interest, under combined bending and pressure loads were evaluated numerically through a procedure based on the principle of virtual work. A solution procedure, originally developed for pure bending loading[11, 29] was extended to include hydrostatic pressure loading.

Kinematics

The problem considered consists of a long, circular, thin-walled tube of mean radius R and wall thickness t (Fig. 10). The tube is in a state of pure bending and external pressure. The tube curvature, κ, and the deformation of its cross section are assumed to be uniform along the tube length. In addition, symmetry about the plane of bending is assumed.

The kinematic relations adopted[10, 30] accommodate relatively large deflections of the tube cross section. The coordinate system used and the displacement components are defined in Fig. 10. It is assumed that plane sections perpendicular to the tube mid-surface and those perpendicular to the tube wall mid-surface remain plane during loading. The strains are assumed to remain small but finite rotations of the plane sections are accommodated.

The circumferential strain can be expressed as

$$\varepsilon_\theta = \varepsilon_\theta^0 + z\kappa_\theta \tag{1}$$

where the membrane component ε_θ^0 is given by

$$\varepsilon_\theta^0 = \left(\frac{v' + w}{R}\right) + \frac{1}{2}\left(\frac{v' + w}{R}\right)^2 + \frac{1}{2}\left(\frac{v - w'}{R}\right)^2 \qquad (2)†$$

and the local curvature κ_θ is given by

$$\kappa_\theta = \left(\frac{v' - w''}{R^2}\right) \Bigg/ \sqrt{\left(1 - \left(\frac{v - w'}{R}\right)^2\right)}. \tag{3}$$

The axial strain can be expressed as

$$\varepsilon_x = \varepsilon_x^0 + \zeta\kappa \tag{4}$$

where ε_x^0 is the axial strain of the axis of the cylinder and

---

† $(\ )' \equiv d(\ )/d\theta$.

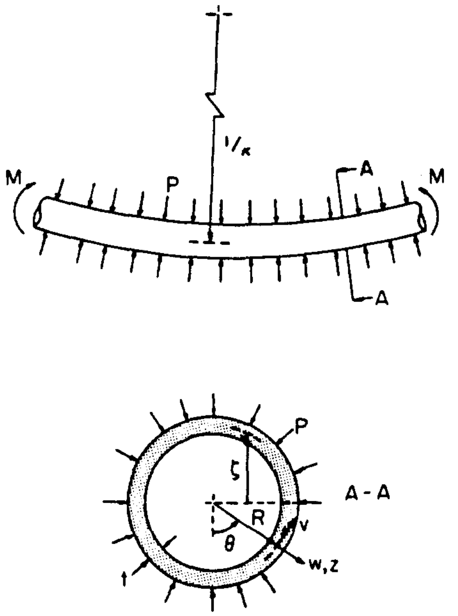

Fig. 10. Problem geometry.

$$\zeta = [(R+w)\cos\theta - v\sin\theta + z\cos\theta] \tag{5}$$

(Fig. 10).

Constitutive behavior

The tube geometries considered, and the particular interest in establishing the sensitivity of the collapse loads to the loading path, dictated that incremental plasticity be used to model the material. The simplifying assumptions of the J_2-type of incremental plasticity are adopted. The customary assumptions of the classical plasticity theory of smooth, convex yield surfaces are adhered to. The strain increment is assumed to be given by

$$\mathrm{d}\varepsilon_{ij} = \mathrm{d}\varepsilon^{e}_{ij} + \mathrm{d}\varepsilon^{p}_{ij}. \tag{6}$$

The elastic part of eqn (6) is assumed to be isotropic and is related to the stress increments through

$$\mathrm{d}\varepsilon^{e}_{ij} = \frac{1}{E}[(1+\nu)\,\mathrm{d}\sigma_{ij} - \nu\,\mathrm{d}\sigma_{kk}\,\delta_{ij}]. \tag{7}$$

Hill's extension of the J_2-type plasticity to anisotropic yielding[31] was used to model the type of anisotropic yielding observed in the tubes used[28]. The stress component normal to the tube wall is assumed negligible and all shear stress components are zero. Thus the equivalent stress is taken as

$$\sigma_e = \left[\sigma_x^2 - \left(1 + \frac{1}{S_\theta^2} - \frac{1}{S_r^2}\right)\sigma_x\sigma_\theta + \frac{1}{S_\theta^2}\sigma_\theta^2\right]^{1/2} \tag{8}$$

where

$$S_\theta = \frac{\sigma_{0\theta}}{\sigma_{0x}}, \quad S_r = \frac{\sigma_{0r}}{\sigma_{0x}}$$

and σ_{0x}, $\sigma_{0\theta}$, σ_{0r} are the initial yield stresses in the principal directions of anisotropy. For the majority of the measurements S_θ and S_r were found to differ only slightly. Thus, unless otherwise stated, the following simplification is adopted:

$$S_\theta = S_r = S. \tag{9}$$

The value of S was obtained from biaxial experiments as described in Ref. [28]. The material stress–strain curves measured experimentally were represented with the three parameter Ramberg–Osgood fit given by

$$\varepsilon = \frac{\sigma}{E}\left[1+\frac{3}{7}\left(\frac{\sigma}{\sigma_y}\right)^{n-1}\right]. \tag{10}$$

The initial yield surface was assumed to be given by

$$\sigma_e = \sigma_{0x}. \tag{11}$$

Subsequent yield surfaces were determined by the flow and hardening rules used. If the yield surface is assumed to grow such that the initial nature of the anisotropy is retained[31] (corresponds to isotropic hardening), then the yield function is defined by

$$f(\sigma) = \sigma_{e\,\max} \tag{12}$$

where $\sigma_{e\,\max}$ represents the largest value of σ_e in the loading history.

The plastic strain increment is given by

$$\mathrm{d}\varepsilon_{ij}^{\mathrm{p}} = \frac{1}{H}\frac{\partial f}{\partial \sigma_{mn}}\,\mathrm{d}\sigma_{mn}\frac{\partial f}{\partial \sigma_{ij}}. \tag{13}$$

For a uniaxial test in the x-direction eqn (13) reduces to

$$H = \frac{\mathrm{d}\sigma_x}{\mathrm{d}\varepsilon_x^{\mathrm{p}}}. \tag{14}$$

This type of model is known to be inappropriate for loading histories which involve reloading preceded by substantial unloading, or involving reverse loading. For some loading histories the problem considered can experience unloading and reloading; thus, the non-linear, kinematic hardening model suggested by Drucker and Palgen[32] was also adopted as an alternative for the analysis. In this case the yield surface retains its initial size but translates in stress space. Subsequent yield surfaces are defined by

$$f(\sigma) = \left[(\sigma_x-\alpha_x)^2-(\sigma_x-\alpha_x)(\sigma_\theta-\alpha_\theta)+\frac{1}{S^2}(\sigma_\theta-\alpha_\theta)^2\right]^{1/2} = \sigma_{0x} \tag{15}$$

where $\boldsymbol{\alpha}$ represents the position of the center of the yield surface in stress space. The model is completed by specifying the direction of translation of the yield surface. The first option used is the one suggested by Ziegler[33] and adopted in Ref. [32]. In this case the yield surface translates in the direction defined by the line joining the current center of the yield surface to the stress point, i.e.

$$\mathrm{d}\alpha_{ij} = \mathrm{d}\mu(\sigma_{ij}-\alpha_{ij}) \tag{16}$$

where the scalar $\mathrm{d}\mu$ is evaluated from the consistency condition.

The second option used was proposed in Ref. [11]. It is based on experimental observations made by Phillips and co-workers as summarized in Ref. [34]. A second surface, given the name the loading surface, representing the maximum state of stress in history was incorporated into the Drucker–Palgen model. This surface is given by

$$F(\sigma) = \sigma_{e\max} \tag{17}$$

it grows in an isotropic fashion whenever the yield surface comes into contact with it. The yield surface is always contained by the loading surface. The two surfaces come into contact tangentially. When the two surfaces are not in contact the yield surface translates in the direction defined by PQ in Fig. 11 (Mroz[35]). This rule ensures that the two surfaces come into contact tangentially.

Principle of virtual work

The principle of virtual work (PVW) is used to satisfy equilibrium. Expressed in terms of the problem variables it can be stated as follows:

$$2R\int_0^{\pi}\int_{-t/2}^{t/2}(\hat{\sigma}_x\delta\dot{\varepsilon}_x+\hat{\sigma}_\theta\delta\dot{\varepsilon}_\theta)\,\mathrm{d}z\,\mathrm{d}\theta$$

$$=\hat{P}R\int_0^{2\pi}\left[\delta\dot{w}+\frac{1}{2R}(2\hat{w}\delta\dot{w}+2\hat{v}\delta\dot{v}+\hat{w}\delta\dot{v}'+\hat{v}'\delta\dot{w}-\hat{v}\delta\dot{w}'-\hat{w}'\delta\dot{v})\right]\mathrm{d}\theta \tag{18}$$

where $\hat{v} = v+\dot{v}$, $\hat{P} = P+\dot{P}$, $\hat{\sigma}_x = \sigma_x+\dot{\sigma}_x$, etc. and $(\dot{\ })$ denotes an increment in ( ). The left-hand side of eqn (18) can be recognized as the increment of work done by the internal stresses and the right-hand side as the increment of external work done by the external pressure. A more detailed form of eqn (18) is given in the Appendix.

The displacement components v and w are approximated by

$$v \simeq R\sum_{n=2}^{N} b_n \sin n\theta,\quad w \simeq R\left[a_0+\sum_{n=1}^{N} a_n \cos n\theta\right]. \tag{19}$$

Equations (19) are substituted in eqns (1)–(5) and those are in turn substituted in eqn (18) as demonstrated in the Appendix. By noting the arbitrariness of

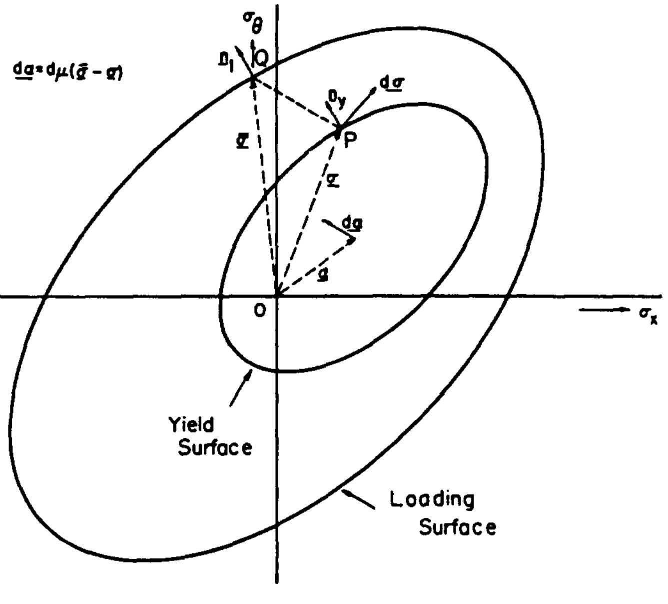

Fig. 11. Two surface hardening rule.

$\{\delta\dot{a}_0, \delta\dot{a}_1, \ldots, \delta\dot{a}_N, \delta\dot{b}_2, \delta\dot{b}_3, \ldots, \delta\dot{b}_N, \delta\dot{\varepsilon}_x^0\}$ a system of $2N+1$ non-linear algebraic equations in terms of $\{\dot{a}_0, \dot{a}_1, \ldots, \dot{a}_N, \dot{b}_2, \dot{b}_3, \ldots, \dot{b}_N, \dot{\varepsilon}_x^0\}$ are obtained. This system of equations is solved using the Newton–Raphson method. The iterative scheme contains nested iterations for the constitutive relations.

The integrations in eqn (18) are carried out numerically using Gaussian quadrature. Seven integration points through the thickness and 12 in the interval $[0, \pi]$ were found to be sufficient through convergence studies[36].

As mentioned earlier bending is controlled by specifying curvature increments $\dot{\kappa}$. Pressure loading is achieved by prescribing either pressure increments, $\dot{P}$ or by prescribing increments of the displacement coefficient a_2 (main contributor to ovality). The displacement controlled approach is required in order to properly identify limit pressures. The values of the loading increments were chosen such that the resultant stress increments did not exceed 2000 psi and the resultant ovality increments ($\Delta D/D$) did not exceed 0.002.

Following a converged solution the values of displacements, strains and stresses are updated and the bending moment evaluated from

$$M = 2R \int_0^{\pi} \int_{-t/2}^{t/2} \sigma_x \zeta \, dz \, d\theta. \tag{20}$$

RESULTS AND DISCUSSIONS

Comparison of experimental and predicted results

The numerical solution procedure described in the previous section was used to simulate the experiments carried out. The main characteristics of the predicted responses for the $\kappa \rightarrow P$ loading path are summarized in a set of results for $D_0/t = 24.5$ presented in Fig. 12.

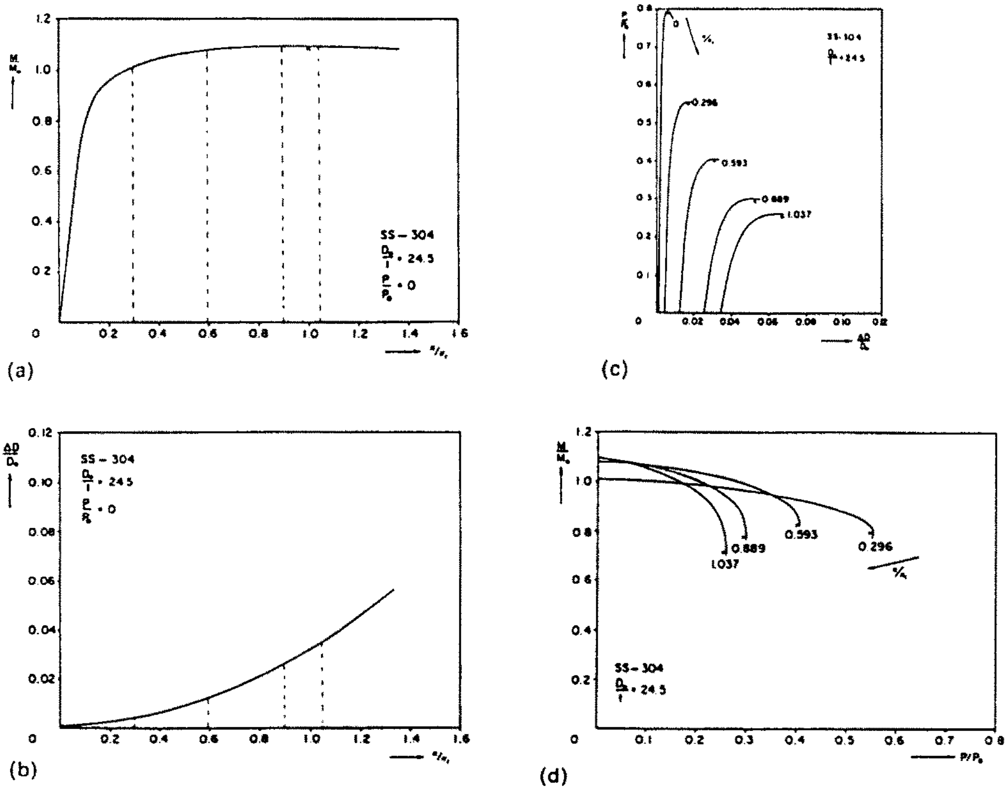

Fig. 12. Calculated responses for the $\kappa \rightarrow P$ loading path: (a) moment–curvature response; (b) ovalization–curvature response; (c) pressure–ovalization responses; (d) moment–pressure responses.

Predicted results for the $P \rightarrow \kappa$ path are presented in Fig. 13. The geometric and material parameters used in these predictions are listed in Table 1. The results are normalized by the following quantities:

$$P_0 = \frac{2\sigma_0 S t}{D_0}, \quad M_0 = \sigma_0 D_0^2 t, \quad \kappa_1 = t/D_0^2. \tag{21}$$

As in the experiments, in the $\kappa \rightarrow P$ loading path the tube was incrementally loaded to the chosen value of curvature at zero pressure. Calculated moment–curvature and ovalization–curvature responses for this part of the path are shown in Figs 12(a) and (b), respectively. The curvature was then fixed (at the four values indicated by dotted lines in the figures) and the pressure incremented. The ovalization developed during the bending part of the path grew further as shown in Fig. 12(c). Eventually a limit pressure was reached. This limit pressure represents the collapse pressure.

During the pressurization process the bending moment drops as shown in Fig. 12(d). This causes material unloading at some points on the cross section, followed by reloading.

The pure bending part of the loading path is curvature controlled and, as a result, the tube does not collapse on the attainment of the limit moment. From experimental observations the ovalization of the tube cross section ceases to be uniform along the length beyond the limit moment. Deformation localizes to a section a few diameters long. This type of deformation cannot be simulated by the analysis described. As a result, the responses predicted beyond the limit moments are in general unconservative.

In the $P \rightarrow \kappa$ loading path pressure was applied first. The pressure–ovalization response for this part of the history is shown in Fig. 13(a). The pressure was then fixed (at the values indicated by dotted lines) and the curvature incremented. The moment-curvature, ovalization-moment and ovalization-curvature responses obtained at four different values

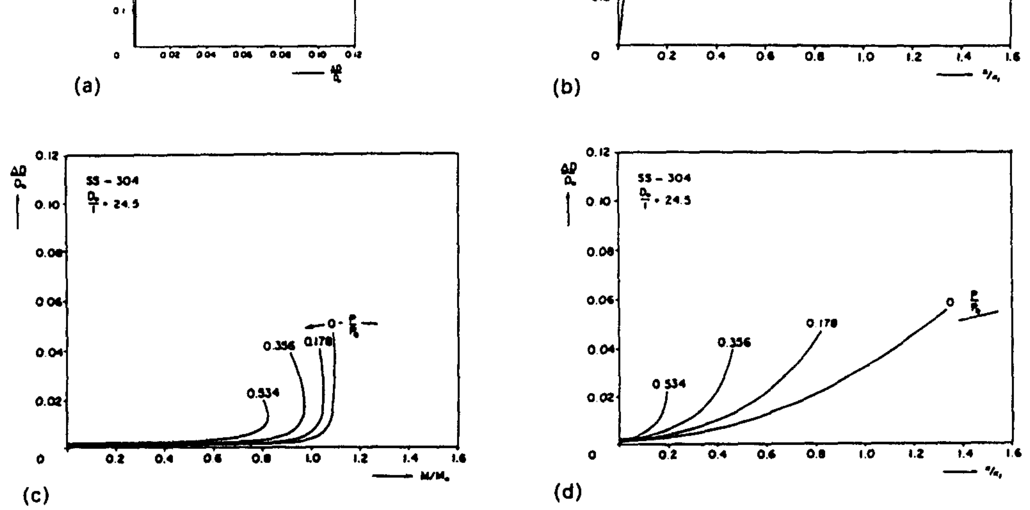

Fig. 13. Calculated responses for the $P \rightarrow \kappa$ loading path: (a) pressure–ovalization response; (b) moment–curvature responses; (c) ovalization–moment responses; (d) ovalization–curvature responses.

of prescribed pressure are shown in Figs 13(b)–(d), respectively. For "lower" values of pressure, the moment–curvature response exhibits a limit moment before collapse. Attainment of the limit moment will be taken as the critical state. The localized deformation which follows the limit moment cannot be simulated by this analysis. As was the case in the experiments, collapse is more clearly identified at "higher" pressures. The critical curvature is identified by a sharp decay in the bending moment with a small increase of curvature. The corresponding ovalization increases sharply to a value at which the external pressure can no longer be supported.

The experimental and predicted values for collapse in the $\kappa \rightarrow P$ loading path for the two D_0/t values considered are shown in Fig. 14. The point on the abscissa represents the curvature at which the limit load occurred under pure bending. The results exhibit a rapid decrease in collapse pressure with increasing curvature up to the value of curvature corresponding to the limit moment. For tubes bent beyond the limit moment, the collapse pressure seems to asymptotically approach a value close to the propagation pressure of the pipe[36]. It is interesting to note that the envelopes do not close in the range of curvatures

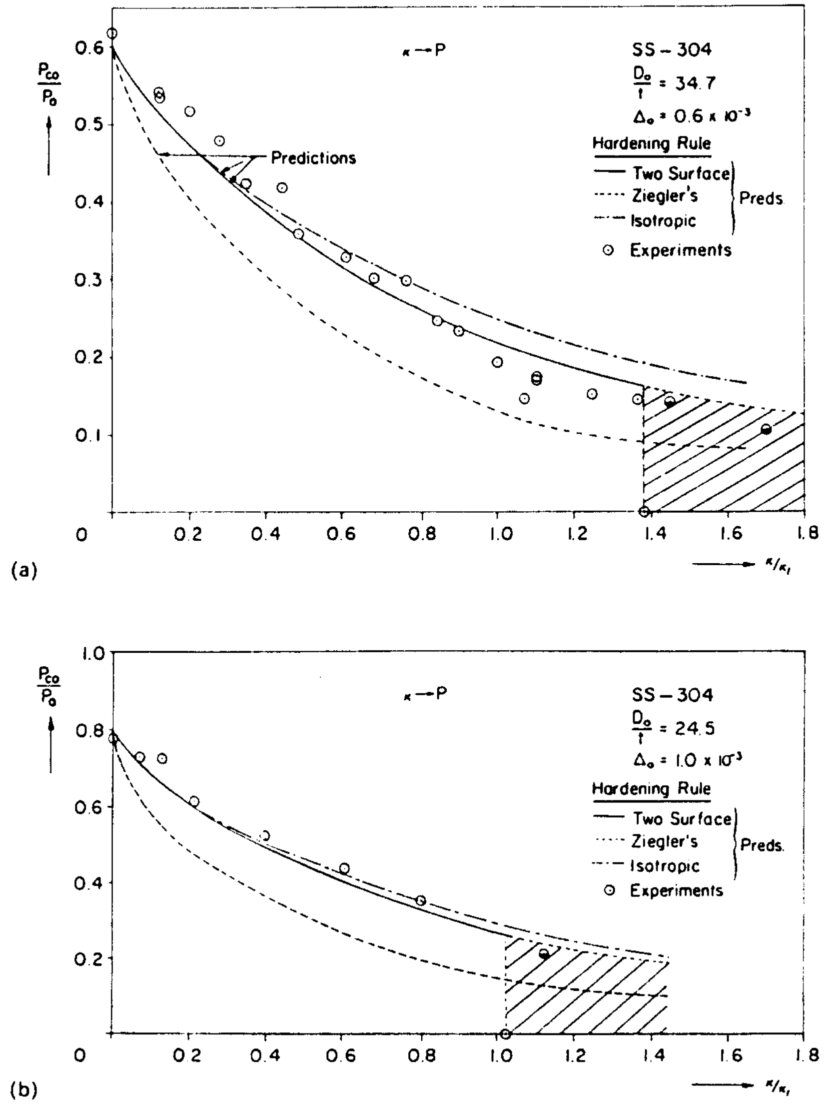

Fig. 14. (a) Comparison of experimental and predicted collapse envelopes for $\kappa \rightarrow P$ path ($D_0/t = 34.7$). (b) Comparison of experimental and predicted collapse envelopes for $\kappa \rightarrow P$ path ($D_0/t = 24.5$).

considered. This is due to the fact that limitations in the testing facility did not allow bending, inside the pressure vessel, up to the point of complete collapse of the tube (e.g. moment capacity reduced to less than 50% of limit moment).

Scatter in the experimental results is due to variations in both geometric and material parameters among the test specimens (i.e. variations not picked up by the normalization used; e.g. variations in initial imperfections, anisotropy, etc.). Predictions based on the mean material and geometric parameters of each D_0/t group are also included in the same plots. Predictions from the three constitutive models described in the previous chapter are included. The same material constants were used in all models. The results from the two-surface hardening rule yield the best overall comparison with the experiments. Isotropic hardening leads to slightly higher results than the two surface kinematic hardening rule and an overestimate of the collapse pressure at higher values of curvature. The results from the kinematic hardening rule with the Ziegler hardening direction substantially underestimate the experimental results.

The main cause for the relative failure of the last model is illustrated in Fig. 15 in which the ovalization predicted by the three models in a pure bending test is compared with experimental values. The Ziegler hardening rule leads to substantially higher predictions for ovalization compared to the other two models which are found to lead to reasonably good agreement with the measured values. Higher ovalization during the bending phase of the loading history results in lower collapse pressures. The main difference between the two kinematic hardening models used is the direction of translation of the yield surface. Sensitivity of predicted stress–strain relationships to the direction of translation of the yield surface were also observed in Refs [11, 37, 38]. These references also showed that the Ziegler hardening direction can lead to unrealistic results.

The pure bending part of the loading path involves no unloading. As a result, the two surface models and the isotropic hardening model yield the same results as demonstrated, for example, in Fig. 15. However, during the pressurization phase of the loading history unloading from and reloading back to a plastic state occurs in some parts of the tube cross section. Figure 16 shows the stress history predicted at a point in the cross section by the two models. The loading history involved pure bending to $\kappa/\kappa_1 = 0.618$ followed by pressurization until collapse. The initial yield surfaces and loading surfaces and the ones at the end of the bending phase are shown. During pressurization unloading occurred and was followed by reloading. For isotropic hardening, plastic reloading was recommended at

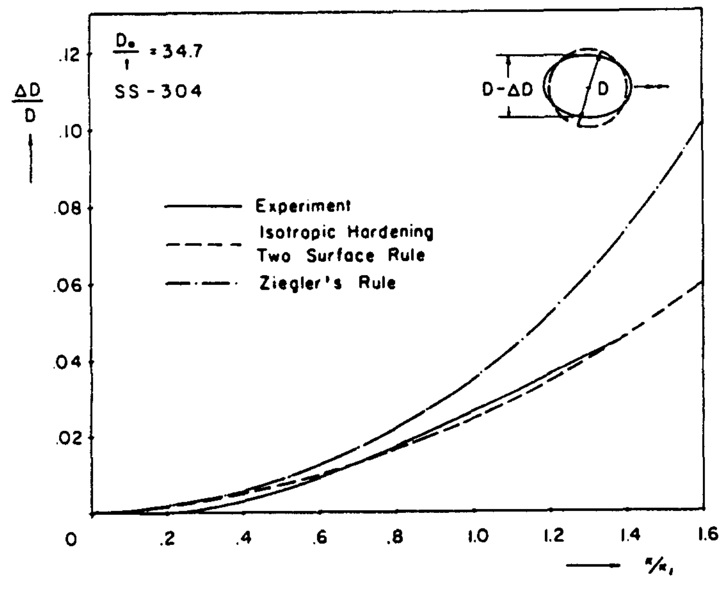

Fig. 15. Measured and predicted ovalizations as a function of curvature (pure bending test).

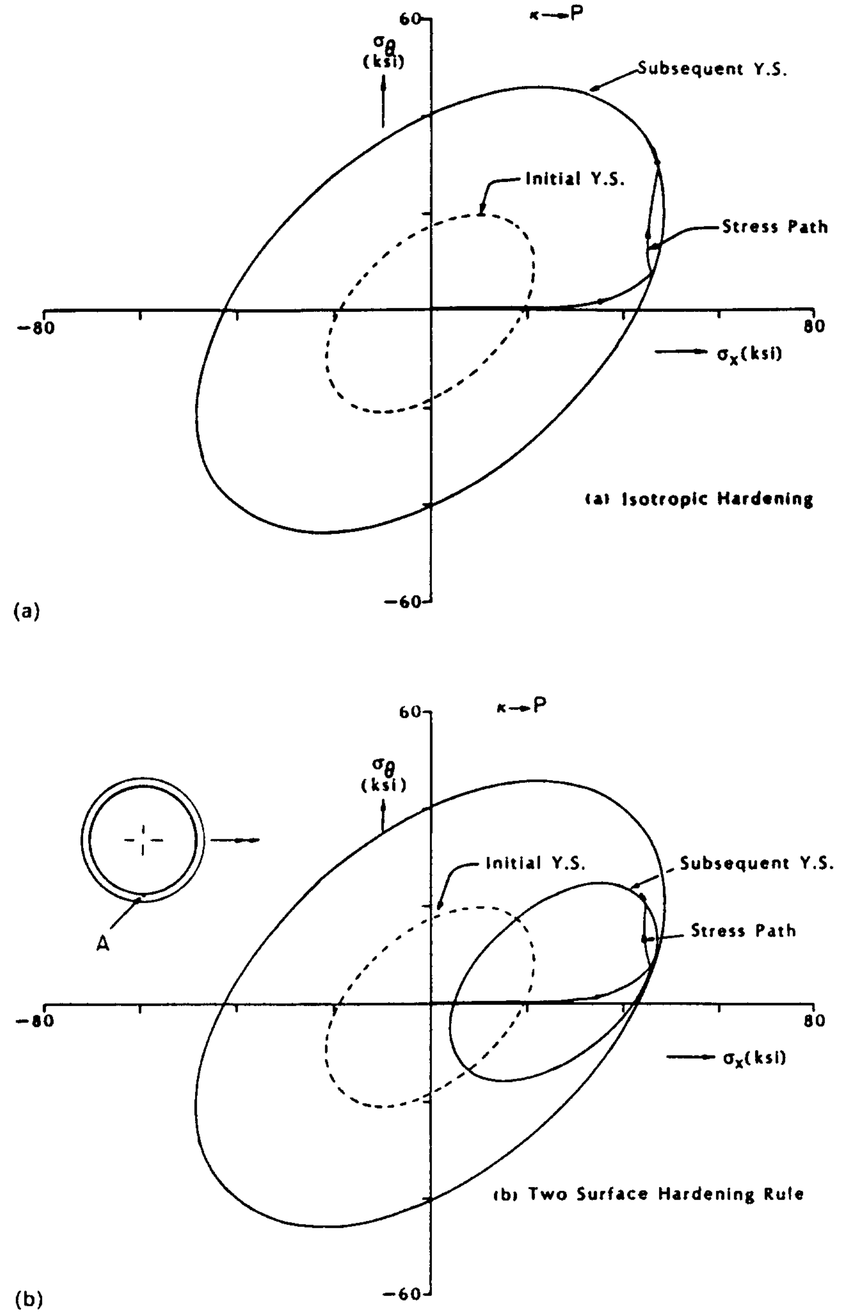

Fig. 16. Stress histories at point "A" predicted by two constitutive models.

$P/P_0 = 0.312$ where as for the two surface rule it was recommended at $P/P_0 = 0.280$. The collapse predicted by the two models occurred at $P/P_0 = 0.316$ and 0.295, respectively.

Isotropic growth leads to an unrealistically large yield surface at the end of the bending phase as shown in Fig. 16(a). This causes delay in the plastic reloading as compared to the two surface hardening rule shown in Fig. 16(b) (indicated by the much larger arc traversed in the elastic range).

The type of behavior described above was characteristic of at least 25% of the integration points. As a result, higher collapse pressures were predicted by isotropic hardening (see Ref. [36] for more details).

Experimental and predicted values for collapse in the $P \rightarrow \kappa$ loading path are shown in Fig. 17. In this case two sets of points are shown. Squares represent the curvatures at

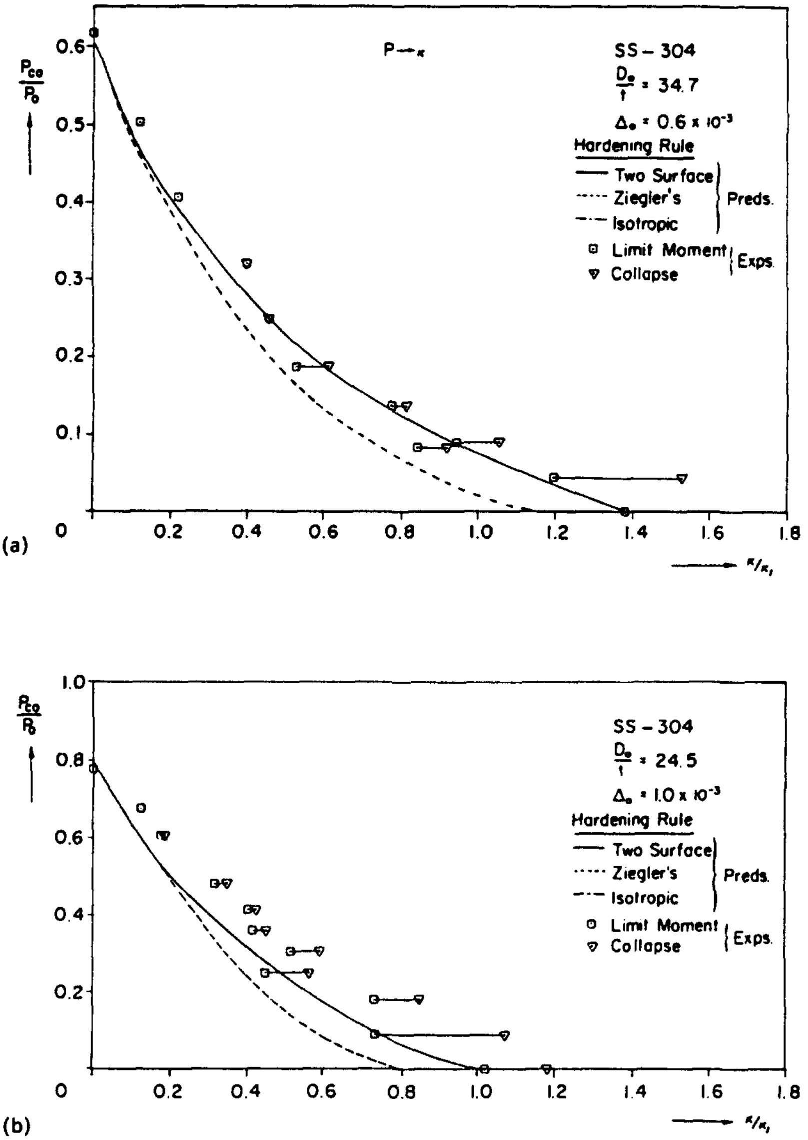

Fig. 17. (a) Comparison of experimental and predicted collapse envelopes for $P \to \kappa$ path ($D_0/t = 34.7$). (b) Comparison of experimental and predicted collapse envelopes for $P \to \kappa$ path ($D_0/t = 24.5$).

which the limit moment was reached; the triangles represent the values at which the tube collapsed catastrophically. At "higher" values of pressure the two failure events are indistinguishable as shown in Fig. 9(a). At "lower" values of pressure the two occurred at increasingly different values. As already mentioned, bending beyond the limit moment was observed to lead to localized deformations. It is again suggested that for design purposes, the curvature at the limit moment should be considered to be the maximum allowable load for the structure.

Predictions of the failure envelopes based on the limit moments are also included in Fig. 17. In this case, the loading history does not involve serious unloading or reloading. As a result the predictions from isotropic hardening and the two surface hardening rule are essentially the same. Good agreement between these predictions and the experimental results is observed for $D_0/t = 34.7$. Reasonable agreement is observed for $D_0/t = 24.5$. In both cases, the kinematic hardening model which incorporates the Ziegler hardening direction, again yields predictions which are substantially lower than the experiments.

The results for the two loading paths and predictions from the two surface hardening

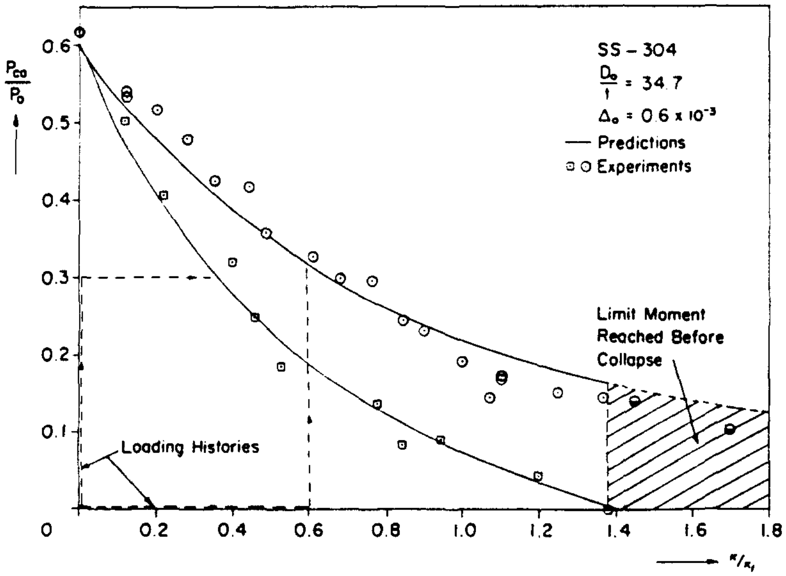

Fig. 18. Collapse envelopes for two loading paths (D_0/t = 34.7).

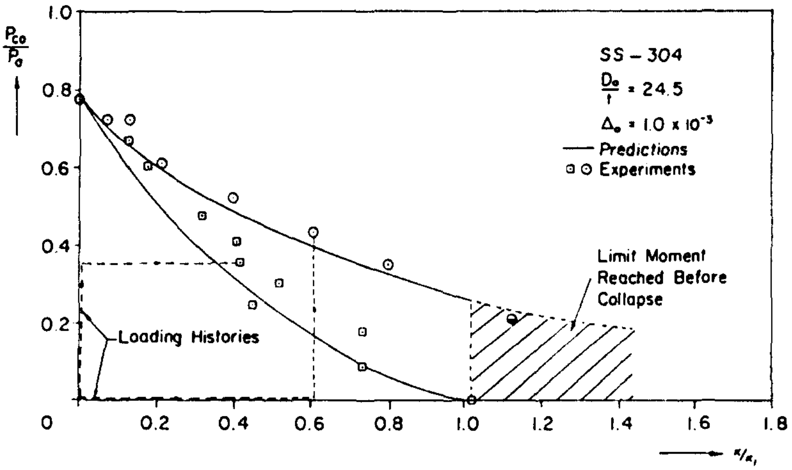

Fig. 19. Collapse envelopes for two loading paths (D_0/t = 24.5).

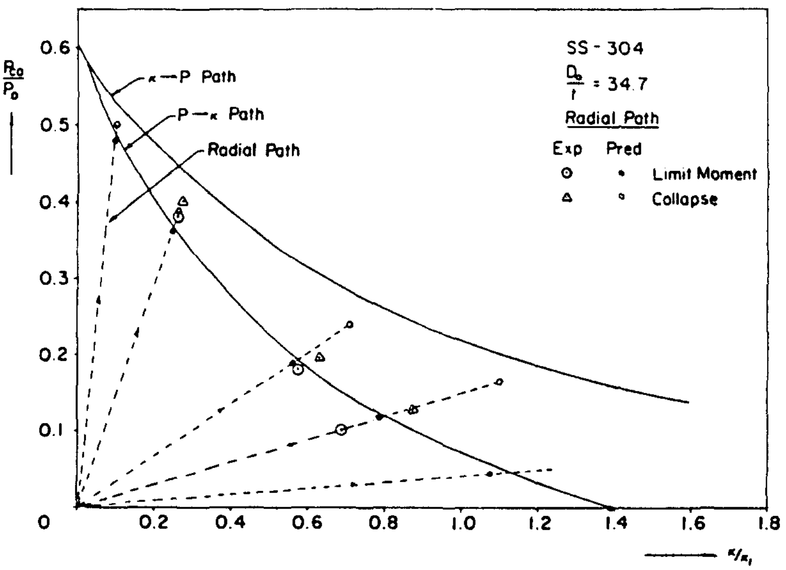

Fig. 20. Comparison of predictions for collapse for radial path and the $\kappa \rightarrow P$ and $P \rightarrow \kappa$ paths.

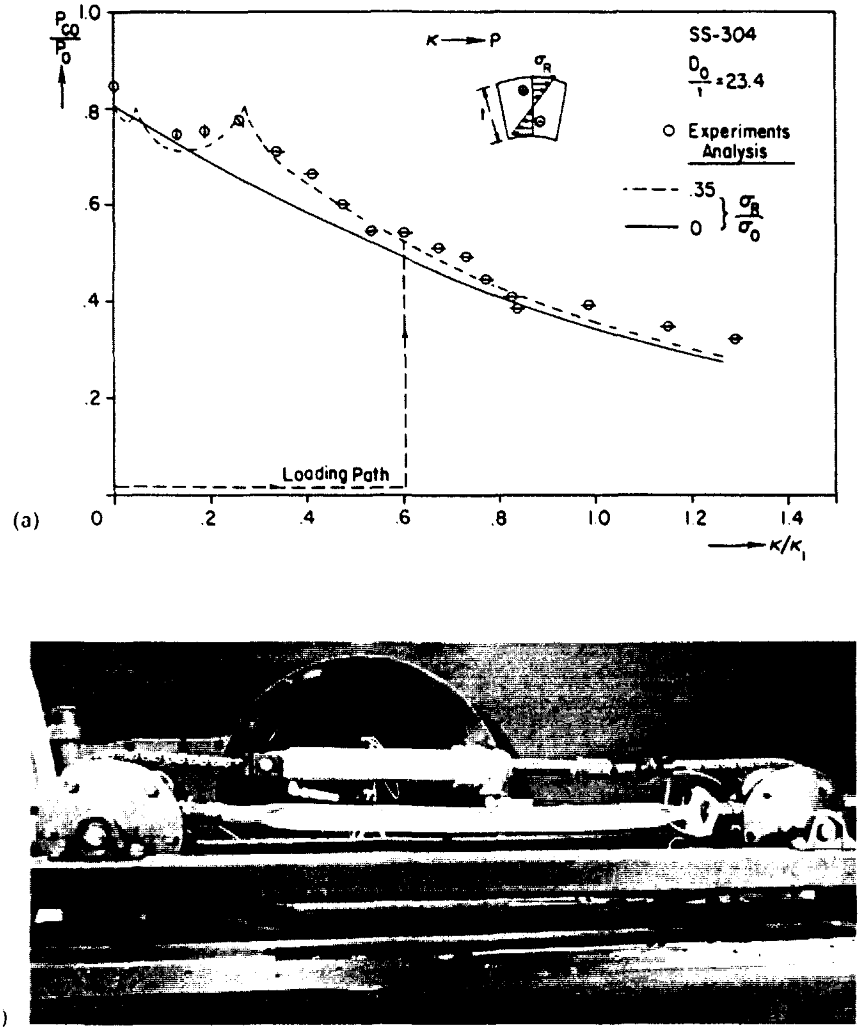

Fig. 21. (a) Collapse pressures as a function of prescribed curvatures in the presence of residual stress field. (b) Reverse collapse mode.

rule model are compared in Fig. 18 for $D_0/t = 34.7$ and Fig. 19 for $D_0/t = 24.5$. The effect of the loading history on catastrophic collapse is clearly demonstrated. In comparing the results for the two loading paths: it is important to remember that the two sets of results were obtained from different, but realistic, failure criteria ($\kappa \rightarrow P$ results represent actual collapse where $P \rightarrow \kappa$ results represent the attainment of a limit moment). However, it is also observed that the $P \rightarrow \kappa$ collapse envelope based on collapse is still substantially lower than the $\kappa \rightarrow P$ envelope. We reiterate that the collapse criteria adopted are the ones considered most suitable for ultimate load design purposes. The main characteristics of the two envelopes seem to be common to both D_0/t values shown.

The primary cause of the lower collapse envelopes for the $P \rightarrow \kappa$ loading history can be attributed to the more severe plastic state induced in the areas of $\theta = 0$, $\pi/2$, π and $3\pi/2$ during loading. This enables an earlier onset of the collapse mechanism which is essentially an $n = 2$ collapse mode.

Results for the third loading path considered which has an approximately radial direction centered at the origin of the $P \rightarrow \kappa$ plane, are shown in Fig. 20. Points at which the limit moment, as well as the actual collapse, occurred are identified for both the experiments as well as the predictions (note that predictions beyond the limit loads are unconservative since localization of deformation is neglected in the analysis). Reasonable agreement between the experimental and predicted limit load cases is observed. It is interesting to observe that the radial path yields critical values which are even lower than the $P \rightarrow \kappa$ path. (Note that in the analysis the path followed was radial whereas in the experiments it was stepwise radial as shown in Fig. 5(c).)

An unusual mode of ovalization

As reported above, bending induces ovalization of the tube cross section. The minor axis of the oval-shaped cross section is usually in the plane of bending. External pressure enhances the growth of the ovalization and leads to the eventual collapse of the tube. The typical mode of collapse obtained in the experiments was as shown in Fig. 8(c); i.e. the tubes collapsed in a plane perpendicular to the plane of bending. In the case of a group of tubes bent to relatively small values of curvature, a different mode of collapse was obtained shown in Fig. 21(b). These tubes collapsed in the plane of bending.

Collapse results, for the $\kappa \rightarrow P$ loading path, obtained from tubes which exhibited this behavior are shown in Fig. 21(a). The mode of collapse is identified by the line drawn through the experimental points. The unusual behavior occurred for bending curvatures, $\kappa/\kappa_1 < 0.3$. In this regime, the collapse pressure measured under increasing prescribed values of curvature, first decreased, then increased and then continued to decrease in the general fashion reported earlier. This behavior was found to be repeatable in a second group of experiments carried out in this curvature regime[39].

Careful measurement of the deformation of the tube cross section in the bending phase of the loading, revealed that, in the curvature regime in question, the tubes exhibited reverse ovalization, i.e. the major axis of the deformed cross section was in the plane of bending[39]. For higher values of bending curvature the induced ovalization returned to the normal type.

Careful consideration of all the problem parameters revealed that bending-induced reverse ovalization, similar to that observed in the experiments, can be caused by the presence of a circumferentially uniform, bending type residual stress. The sense of the residual bending stress required is such that if the tube is cut along a generator it would spring open (Fig. 21(a)). The range of curvature in which reverse ovalization is exhibited and its amplitude depend on the strength of the residual stress field (i.e. σ_R/σ_0). Experiments carried out on the tubes used in the collapse tests verified that the major component of the residual stress field was of this type.

Figure 21(a) shows analytical predictions of the $\kappa \rightarrow P$ collapse envelope including a residual stress field of the type described of strength $\sigma_R/\sigma_0 = 0.35$. At low values of curvature the collapse envelope exhibits two cusps. The predicted collapse mode for curvature values between the two cusps was found to be of the unusual type. The agreement between the experimental and predicted results is good for all values of curvatures.

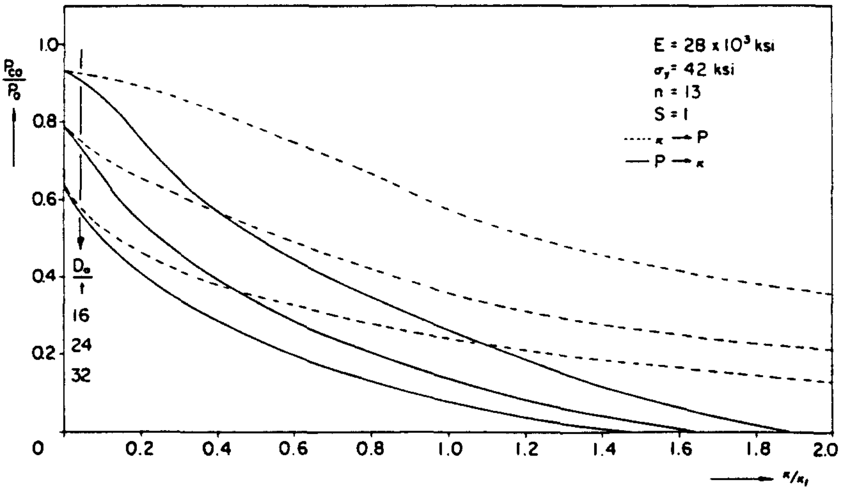

Fig. 22. Predicted collapse envelopes for three different D_0/t values.

Results predicted without including residual stresses are also included for comparison purposes.

Parametric study

The suitability of the problem formulation and the solution procedure used in predicting the limit load type of instabilities, which characterize the problem in the low D_0/t range, has been demonstrated. In this section, the numerical solution procedure was used to examine the dependence of the collapse envelopes on various problem parameters. Collapse envelopes for the $\kappa \rightarrow P$ and $P \rightarrow \kappa$ loading paths were generated for each parameter varied. The collapse criteria adopted are the same as those identified in the previous section.

Figure 22 shows the predicted collapse envelopes for D_0/t values of 32, 24 and 16. The main characteristics of the three envelopes remain the same. As expected, tubes with lower D_0/t values can sustain higher combinations of pressure and curvature.

The effect of small initial geometric imperfections on the collapse envelopes is examined in Fig. 23. The geometry of the imperfection used was as follows:

$$w_0(\theta) = -R\Delta_0 \cos 2\theta. \tag{22}$$

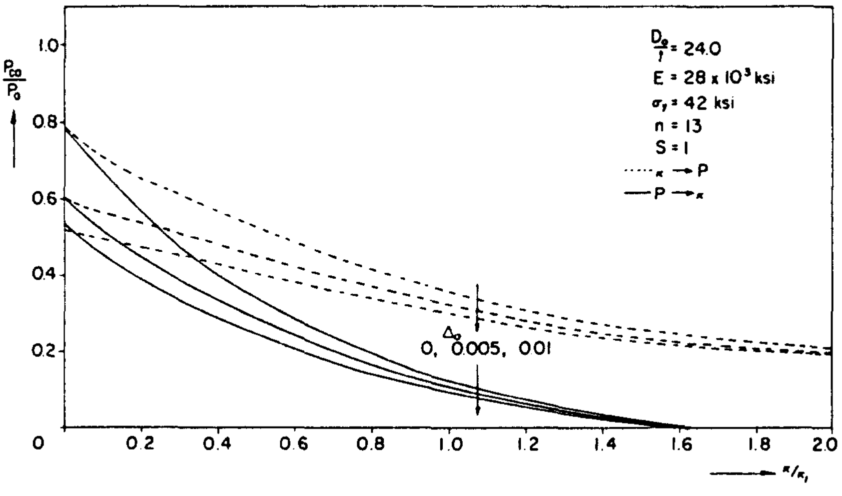

Fig. 23. Predicted collapse envelopes for tubes with initial imperfections.

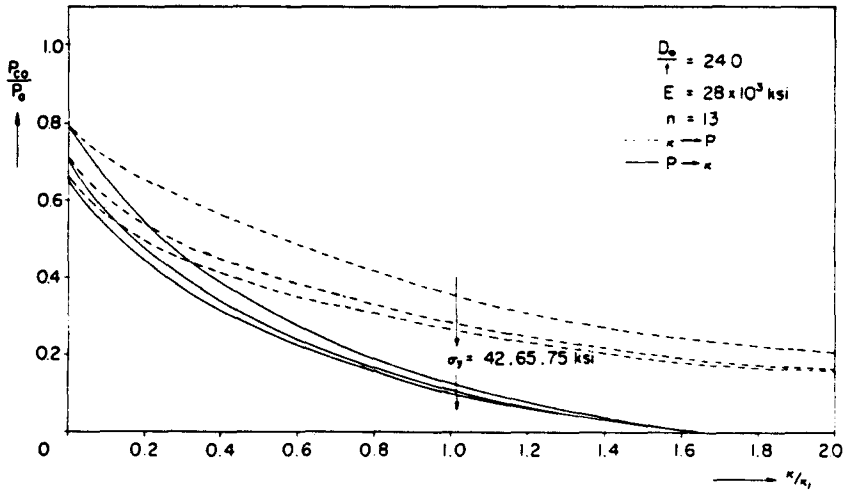

Fig. 24. Predicted collapse envelopes for different values of σ_y.

Collapse under pure pressure is very sensitive to imperfections as reported in Ref. [21] and elsewhere. The curvature corresponding to the limit moment is relatively insensitive to such imperfections. As a result, the predicted load combinations at failure are lower in the presence of imperfections for low curvatures. At higher curvatures the effect of this type of imperfection is less pronounced.

Figure 24 shows how the collapse envelopes vary with the material yield parameter σ_y. It is important to note that in each case shown the normalizing pressure P_0 was adjusted to reflect the change in σ_y. Thus, the seemingly higher predicted collapse pressures shown in the figure for lower yield stresses are due to the normalization used. If the tube has a collapse pressure which is influenced by inelastic effects, then an increase in the yield stress will cause an increase in the collapse pressure. It is interesting to observe that in the pure bending case the curvature corresponding to the limit moment does not vary in the range of yield stresses considered.

Figure 25 shows the variation of the collapse envelopes with the material anisotropy parameter S. The material exhibits isotropic yielding if $S = 1$. When $S < 1$ the yield stress in the circumferential direction is lower than that in the axial direction. The normalizing pressure P_0 reflects changes in S; thus, again, the effect of anisotropy on the collapse

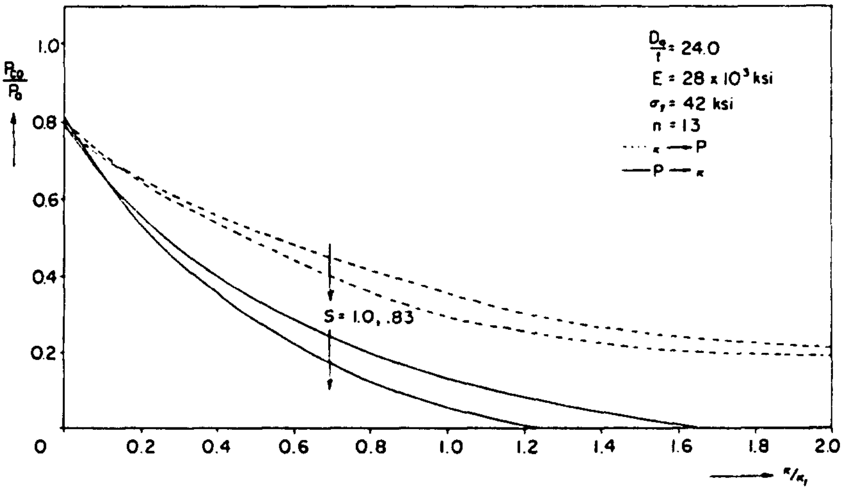

Fig. 25. Effect of yield anisotropy on predicted collapse envelopes.

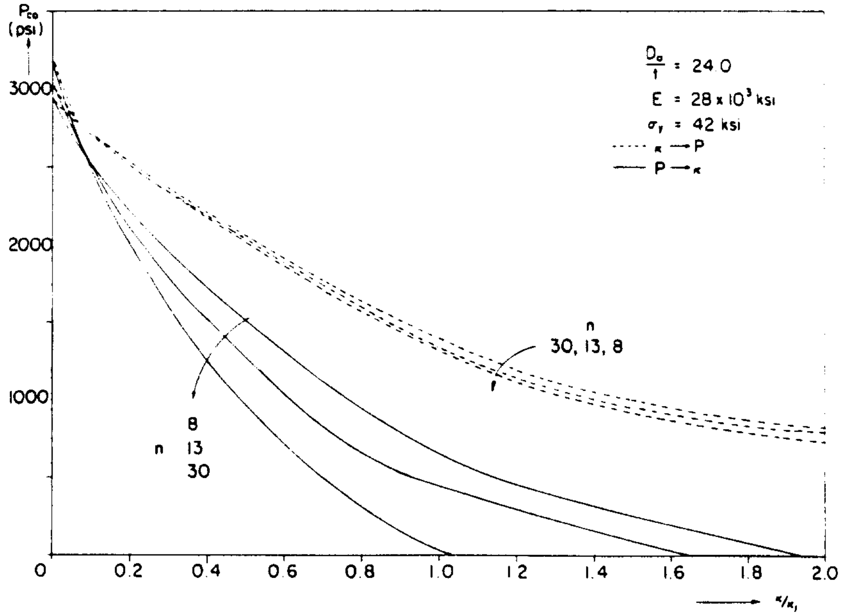

Fig. 26. Effect of material hardening parameter on predicted collapse envelopes.

pressure (vertical axis) is normalized out. However, it can be stated that anisotropy in which $S < 1$ leads to lower collapse loads.

Figure 26 shows how the material hardening parameter n affects the collapse envelopes. It is observed that the hardening parameter has a very small effect on the collapse envelope for the $\kappa \rightarrow P$ loading path but a much bigger effect on the $P \rightarrow \kappa$ envelope. The seemingly unusual results at low values of curvature, are due to the shape of the Ramberg–Osgood stress–strain fit at low strain values.

SUMMARY AND CONCLUSIONS

The response and stability of long, relatively thick-walled steel tubes was studied through a combined experimental and numerical program. Stainless steel 304 tubes with D_0/t values of 34.7 and 24.5 were loaded to collapse. Pressure–curvature collapse envelopes were generated for loading paths involving bending followed by pressurization, and pressurization followed by bending. A limited number of experiments involving a radial loading path were also carried out. The material properties of the test specimen were measured in separate experiments. The material and geometric properties of the tubes tested were such that significant plastic deformations were induced by the loading applied.

The responses of the tubes were found to be characterized by limit load type of instabilities for all loading paths examined. Under pure pressure loading, the tubes tested catastrophically collapsed on attaining a limit pressure (loading essentially pressure controlled). Under pure bending loading the tubes were found to attain a limit moment. Due to the curvature controlled loading used, bending could be continued beyond the limit moment. Following the limit load, the tube deformation (ovalization of cross-section) localized to a region a few diameters long. Continued bending led to a precipitous drop in bending capacity.

When bending and pressure were applied simultaneously, the collapse pressure, the maximum bending moment capacity and the corresponding curvature were reduced due to the interaction of geometric and material nonlinearities. Geometrically, the two loads interact through the tube ovalization. The material interaction occurs through inelastic effects. Since the latter are path dependent, both the response as well as the instabilities of the tubes were found to depend on the loading path.

In the $\kappa \rightarrow P$ loading path the collapse was due to a limit load type of instability in the pressure response. In the small curvature range the collapse pressure dropped relatively quickly with increasing bending curvature. For larger curvatures the collapse pressure seems to asymptotically approach the propagation pressure of the pipe.

In the $P \to \kappa$ loading path two types of instabilities were observed. A limit moment in the response and catastrophic collapse. At higher pressures the two were indistinguishable. At lower pressures a limit moment was reached first followed by localization in the tube ovalization which eventually led to catastrophic collapse of the tube.

The results from the radial path were similar to those of the $P \to \kappa$ path.

Attainment of a limit load was chosen as the instability criterion most appropriate for the problem in the low D_0/t range studied. A formulation of the problem in which all variables remain constant along the tube length was used to predict the tube response and limit load type of instability. The J_2 incremental theory of plasticity, with three different hardening rules, was used to model the material inelastic behavior. The predictions were found to be sensitive to the hardening rule used. A two surface hardening rule developed was found to yield the best agreement with experiments. Isotropic hardening tended to overestimate the collapse pressures in the large curvature range for the $\kappa \to P$ loading path. Ziegler type kinematic hardening was found to lead to unrealistically low predictions of the collapse loads.

In general the experimental results can be numerically reproduced provided the geometric and material parameters of the problem are carefully measured. These must include mean values of the tube initial ovalization, the material stress–strain behavior, anisotropic yielding and circumferential residual stresses.

Acknowledgements—The work presented was carried out with the financial assistance of the American Gas Association (AGA) (Contract No. PR-106-521) and the National Science Foundation (NSF) (Grant No. MSM8352370). This financial assistance is gratefully acknowledged. Opinions, findings, conclusions and recommendations expressed herein are those of the authors and do not necessarily reflect the views of the AGA and NSF.

REFERENCES

1. C. E. Murphey and C. G. Langer, Ultimate pipe strength under bending, collapse and fatigue. 4th Int. Offshore and Arctic Engineering Symposium, Vol. 1, p. 467 (1985).
2. L. G. Brazier, On the flexure of thin cylindrical shells and other thin sections. *Proc. R. Soc.* **A116,** 104 (1927).
3. E. Reissner and H. J. Weinitschke, Finite pure bending of circular cylindrical tubes. *Q. Appl. Math.* **20,** 305 (1963).
4. E. L. Axelrad, Flexible shells. *Proc. 15th IUTAM*, Toronto, Canada, pp. 45–56, August (1980).
5. P. Seide and V. I. Weingarden, On the buckling of circular cylindrical shells under pure bending. *ASME J. Appl. Mech.* **28,** 112 (1961).
6. W. B. Stephens, J. H. Starnes and B. O. Almroth, Collapse of long cylindrical shells under combined bending and pressure loads. *AIAA J.* **13,** 2025 (1975).
7. O. Fabian, Collapse of cylindrical, elastic tubes under combined bending, pressure and axial loads. *Int. J. Solids Structures* **13,** 1257 (1977).
8. F. A. Emmerling, Nonlinear bending of elliptic tubes under normal pressure. *Ingenieur-Arch.* **52,** 1–16 (1982).
9. C. S. Ades, Bending strength of tubing in the plastic range. *J. Aeronaut. Sci.* **24,** 605 (1957).
10. S. Gellin, The plastic buckling of long cylindrical shells under pure bending. *Int. J. Solids Structures* **10,** 397 (1980).
11. P. K. Shaw and S. Kyriakides, Inelastic analysis of thin-walled tubes under cyclic bending. *Int. J. Solids Structures* **21,** 1073 (1985).
12. D. Bushnell, Elastic plastic bending and buckling of pipes and elbows. *Comput. Struct.* **13,** 241 (1981).
13. C. R. Calladine, Plastic buckling of tubes in pure bending. *Proc. IUTAM Conf. on Collapse* (Edited by G. W. Hunt and J. M. T. Thompson), p. 111. London, U.K. (1983).
14. R. L. Moore and J. W. Clark, Torsion, compression, and bending of tubular sections machined from 755-T6 rolled round rod. NACA RM 52125 (1952).
15. J. E. Jirsa, F. H. Lee, J. C. Wilhoit and J. E. Merwin, Ovaling of pipelines under pure bending, OTC 1569. *Proc. Offshore Tech. Conf.*, Vol. I, p. 573 (1972).
16. D. R. Sherman, Tests of circular steel tubes in bending. *ASCE J. Struct. Div.* **102**(ST11), 2181 (1976).
17. P. Tuggu and J. Schroeder, Plastic deformation and stability of pipes exposed to external couples. *Int. J. Solids Structures* **15,** 643 (1979).
18. B. D. Reddy, An experimental study of the plastic buckling of circular cylinders in pure bending. *Int. J. Solids Structures* **15,** 669 (1979).
19. R. M. Korol, Critical buckling strains of round tubes in flexure. *Int. J. Mech. Sci.* **21,** 719 (1979).
20. S. Kyriakides and P. K. Shaw, Inelastic buckling of tubes under cyclic loads. *ASME J. Press. Vessel Technol.* **109,** 169 (1987).
21. M. K. Yeh and S. Kyriakides, On the collapse of inelastic thick-walled tubes under external pressure. *ASME J. Engng Resour. Technol.* **108,** 35 (1986).

22. M. K. Yeh and S. Kyriakides, Collapse of deepwater pipelines, OTC 5215. *Proc. Offshore Tech. Conf.*, Vol. III, p. 511 (1986).
23. T. G. Johns, R. E. Mesloh, R. Winegardner and J. E. Sorenson, Inelastic buckling of pipelines under combined loads, OTC 2209. *Proc. Offshore Tech. Conf.*, Vol. II, p. 635 (1975).
24. S. Kyriakides, On the stability of inelastic circular pipes under combined bending and external pressure. *Proc. Spring Meeting, Society of Experimental Stress Analysis*, Dearborn, Michigan, p. 372 (1981).
25. S. Kyriakides and P. K. Shaw, Response and stability of elastoplastic circular pipes under combined bending and external pressure. *Int. J. Solids Structures* **18**, 957 (1982).
26. O. Fabian, Elastic–plastic collapse of long tubes under combined bending and pressure loads. *Ocean Engng* **8**, 295 (1981).
27. P. E. De Winter, J. W. B. Stark and J. Witteveen, Collapse behaviour of submarine pipelines. In *Shell Structures: Stability and Strength* (Edited by R. Narayanan), Chap. 7, p. 221. Elsevier, Amsterdam (1985).
28. S. Kyriakides and M. K. Yeh, Plastic anisotropy in drawn tubes, Engineering Mechanics Research Laboratory, Report EMRL 86/11. *ASME J. Engng Ind.* (1988), in press.
29. P. K. Shaw, On the ovalization of inelastic tubes under cyclic bending. Ph.D. Thesis, University of Texas at Austin (1985).
30. D. O. Brush and B. O. Almroth, *Buckling of Bars, Plates and Shells*. McGraw-Hill, New York (1975).
31. R. Hill, *The Mathematical Theory of Plasticity*. Oxford University Press, Oxford (1950).
32. D. C. Drucker and L. Palgen, On stress–strain relations suitable for cyclic and other loadings. *ASME J. Appl. Mech.* **48**, 479 (1981).
33. H. Ziegler, A modification of Prager's hardening rule. *Q. Appl. Math.* **17**, 55 (1959).
34. A. Phillips and C. W. Lee, Yield surfaces and loading surfaces: experiments and recommendations. *Int. J. Solids Structures* **15**, 715 (1979).
35. Z. Mroz, On the description of anisotropic workhardening. *J. Mech. Phys. Solids* **15**, 163 (1967).
36. E. Corona, Stability of long elastoplastic circular tubes under combined bending and pressure. M.S. Thesis, University of Texas at Austin, EMRL Rep. No. 86/7, August (1986).
37. E. Shiratory, K. Ikegami and R. Yoshida, Analysis of stress–strain relations by use of an anisotropic hardening plastic potential. *J. Mech. Phys. Solids* **27**, 213 (1979).
38. H. S. Lamba and O. M. Sidebottom, Cyclic plasticity for nonproportional paths: Part 2—comparison with predictions of three incremental plasticity models. *ASME J. Engng Mater. Technol.* **100**, 104 (1978).
39. E. Corona and S. Kyriakides, An unusual mode of collapse of tubes under combined bending and pressure. *ASME J. Press. Vessel Technol.* **109**, 302 (1987).

APPENDIX

The set of $2N+1$ non-linear algebraic equations used to find the solution can be derived as follows: from the kinematic relations (1)–(5) we obtain

$$\delta\dot{\varepsilon}_x = \delta\dot{\varepsilon}_x^0 + \dot{\kappa}(\delta\dot{w}\cos\theta - \delta\dot{v}\sin\theta) \tag{A1}$$

$$\delta\dot{\varepsilon}_\theta = \delta\dot{\varepsilon}_\theta^0 + z\delta\dot{\kappa}_\theta \tag{A2}$$

$$\delta\dot{\varepsilon}_\theta^0 = \frac{1}{R^2}\left[(R+\dot{v}'+\dot{w})(\delta\dot{v}'+\delta\dot{w}) + (\dot{v}-\dot{w}')(\delta\dot{v}-\delta\dot{w}')\right] \tag{A3}$$

$$\delta\dot{\kappa}_\theta = \frac{1}{R^2}\,\frac{\left[1-\left(\dfrac{\dot{v}-\dot{w}'}{R}\right)^2\right](\delta\dot{v}'-\delta\dot{w}'') + (\dot{v}'-\dot{w}'')(\dot{v}-\dot{w}')\left(\dfrac{\delta\dot{v}-\delta\dot{w}'}{R^2}\right)}{\left[1-\left(\dfrac{\dot{v}-\dot{w}'}{R}\right)^2\right]^{3/2}}. \tag{A4}$$

Substituting eqns (19) into the above equations

$$\delta\dot{\varepsilon}_x = \delta\dot{\varepsilon}_x^0 + (R\dot{\kappa}\cos\theta)\delta\dot{a}_0 + \sum_{n=1}^{N}(R\dot{\kappa}\cos n\theta\cos\theta)\delta\dot{a}_n - \sum_{n=2}^{N}(R\dot{\kappa}\sin n\theta\sin\theta)\delta\dot{b}_n \tag{A5}$$

$$\begin{aligned}\delta\dot{\varepsilon}_\theta^0 = \frac{1}{R}\Bigg\{&(R+\dot{v}'+\dot{w})\delta\dot{a}_0 + (R+\dot{v}'+\dot{w})\sum_{n=1}^{N}\delta\dot{a}_n\cos n\theta \\ &+(\dot{v}-\dot{w}')\sum_{n=1}^{N}\delta\dot{a}_n n\sin n\theta + (R+\dot{v}'+\dot{w})\sum_{n=2}^{N}\delta\dot{b}_n n\cos n\theta + (\dot{v}-\dot{w}')\sum_{n=2}^{N}\delta\dot{b}_n\sin n\theta\Bigg\}\end{aligned} \tag{A6}$$

$$\begin{aligned}\delta\dot{\kappa}_\theta = {}&\frac{\displaystyle\sum_{n=1}^{N}\delta\dot{a}_n n^2\cos n\theta + \sum_{n=2}^{N}\delta\dot{b}_n n\cos n\theta}{R\sqrt{\left(1-\left(\dfrac{\dot{v}-\dot{w}'}{R}\right)^2\right)}} \\ &+\frac{\displaystyle(\dot{v}'-\dot{w}'')(\dot{v}-\dot{w}')\sum_{n=1}^{N}\delta\dot{a}_n n\sin n\theta + (\dot{v}'-\dot{w}'')(\dot{v}-\dot{w}')\sum_{n=2}^{N}\delta\dot{b}_n\sin n\theta}{R^3\left[1-\left(\dfrac{\dot{v}-\dot{w}'}{R}\right)^2\right]^{3/2}}.\end{aligned} \tag{A7}$$

Substituting eqns (A5)–(A7) in the principle of virtual work and observing the arbitrariness of $\delta\dot{a}_0$, $\delta\dot{a}_n$, $\delta\dot{b}_n$, and $\delta\dot{\varepsilon}_x^0$, the following system of non-linear algebraic equations is obtained

$$f_0 = R\int_0^{\pi}\int_{-t/2}^{t/2}\left[\dot{\sigma}_x(R\dot{\kappa}\cos\theta)+\frac{\dot{\sigma}_\theta}{R}(R+\dot{v}'+\dot{w})\right]\mathrm{d}z\,\mathrm{d}\theta+\dot{P}R^2\pi(\dot{a}_0+1)=0$$

$$\begin{aligned}f_n = R\int_0^{\pi}\int_{-t/2}^{t/2}\Bigg\{&\dot{\sigma}_x[R\dot{\kappa}\cos n\theta\cos\theta]+\frac{\dot{\sigma}_\theta}{R}\Bigg[(R+\dot{v}'+\dot{w})\cos n\theta+(\dot{v}-\dot{w}')n\sin n\theta\\&+\frac{z}{R}\left[\frac{n^2\cos n\theta}{\sqrt{\left(1-\left(\frac{\dot{v}-\dot{w}'}{R}\right)^2\right)}}+\frac{(\dot{v}'-\dot{w}'')(\dot{v}-\dot{w}')n\sin n\theta}{R^2\left[1-\left(\frac{\dot{v}-\dot{w}'}{R}\right)^2\right]^{3/2}}\right]\Bigg]\Bigg\}\mathrm{d}z\,\mathrm{d}\theta+\tfrac{1}{2}\dot{P}R^2\pi(\dot{a}_n+n\dot{b}_n)=0\end{aligned}$$

for $1\leqslant n\leqslant N$

$$\begin{aligned}f_n = R\int_0^{\pi}\int_{-t/2}^{t/2}\Bigg\{&\dot{\sigma}_x[-R\dot{\kappa}\sin(n-N)\theta\sin\theta]\\&+\frac{\dot{\sigma}_\theta}{R}\Bigg[(R+\dot{v}'+\dot{w})(n-N)\cos(n-N)\theta+(\dot{v}-\dot{w}')\sin(n-N)\theta\\&+\frac{z}{R}\left[\frac{(n-N)\cos(n-N)\theta}{\sqrt{\left(1-\left(\frac{\dot{v}-\dot{w}'}{R}\right)^2\right)}}+\frac{(\dot{v}'-\dot{w}'')(\dot{v}-\dot{w}')\sin(n-N)\theta}{R^2\left[1-\left(\frac{\dot{v}-\dot{w}'}{R}\right)^2\right]^{3/2}}\right]\Bigg]\Bigg\}\mathrm{d}z\,\mathrm{d}\theta\\&+\tfrac{1}{2}\dot{P}R^2\pi(\dot{b}_{n-N}+(n-N)\dot{a}_{n-N})=0\end{aligned}$$

for $N+2\leqslant n\leqslant 2N$

$$f_{2N+1} = R\int_0^{\pi}\int_{-t/2}^{t/2}\dot{\sigma}_x\,\mathrm{d}z\,\mathrm{d}\theta=0. \qquad \text{(A8)}$$